



# *Capturing uncertainty in magnetospheric ultra-low frequency wave models*

Article

Accepted Version

Bentley, S. N., Watt, C. E. J., Rae, I. J., Owens, M. J., Murphy, K., Lockwood, M. and Sandhu, J. K. (2019) Capturing uncertainty in magnetospheric ultra-low frequency wave models. *Space Weather*, 17 (4). pp. 599-618. ISSN 1542-7390 doi: <https://doi.org/10.1029/2018SW002102> Available at <http://centaur.reading.ac.uk/82678/>

It is advisable to refer to the publisher's version if you intend to cite from the work. See [Guidance on citing](#).

To link to this article DOI: <http://dx.doi.org/10.1029/2018SW002102>

Publisher: American Geophysical Union

All outputs in CentAUR are protected by Intellectual Property Rights law, including copyright law. Copyright and IPR is retained by the creators or other copyright holders. Terms and conditions for use of this material are defined in the [End User Agreement](#).

[www.reading.ac.uk/centaur](http://www.reading.ac.uk/centaur)

**CentAUR**

Central Archive at the University of Reading

Reading's research outputs online

# Capturing uncertainty in magnetospheric ultra-low frequency wave models

S.N.Bentley<sup>1</sup>, Clare E. J. Watt<sup>1</sup>, I.J.Rae<sup>2</sup>, M.J.Owens<sup>1</sup>, K.Murphy<sup>3</sup>, M.Lockwood<sup>1</sup>,  
J.K.Sandhu<sup>2</sup>

<sup>1</sup>University of Reading, UK

<sup>2</sup>MSSL, UCL, UK

<sup>3</sup>University of Maryland Department of Astronomy, USA

## Key Points:

- Determining uncertainty in wave power models is necessary to quantify uncertainty in radial diffusion coefficients for modeling.
- Our model of ground-based ULF wave power depends on solar wind speed, number density variance and  $B_z$ . This outperforms hourly persistence.
- Total power over extended events is best modeled probabilistically while the wave power in a single hour is best modeled deterministically.

---

Corresponding author: S. N. Bentley, [snbentley@outlook.com](mailto:snbentley@outlook.com)

**Abstract**

We develop and test an empirical model predicting ground-based observations of ultra-low frequency (ULF, 1-20 mHz) wave power across a range of frequencies, latitudes and magnetic local time sectors. This is parameterized by instantaneous solar wind speed  $v_{sw}$ , variance in proton number density  $var(Np)$  and interplanetary southward magnetic field  $B_z$ . A probabilistic model of ULF wave power will allow us to address uncertainty in radial diffusion coefficients and therefore improve diffusion modeling of radial transport in Earth's outer radiation belt. Our model can be used in two ways to reproduce wave power; by sampling from conditional probability distribution functions or by using the mean (expectation) values. We derive a method for testing the quality of the parameterization and test the ability of the model to reproduce ULF wave power time series. Sampling is a better method for reproducing power over an extended time period as it retains the same overall distribution while mean values are better for predicting the power in a time series. The model predicts each hour in a time series better than the assumption that power persists from the preceding hour. Finally, we review other sources of diffusion coefficient uncertainty. Although this wave model is designed principally for the goal of improved radial diffusion coefficients to include in outer radiation belt diffusion based modeling, we anticipate that our model can also be used to investigate the occurrence of ULF waves throughout the magnetosphere and hence the physics of ULF wave generation and propagation.

**1 Introduction**

Modeling of the outer radiation belt can potentially enable satellite operators to protect their spacecraft from dangerous space weather such as spacecraft charging, deep dielectric charging and single upset events [Baker *et al.*, 1987; Frederickson, 1996; Horne *et al.*, 2013]. One of the areas identified as requiring better characterization in order to improve forecasting and modeling of past events is the radial transport of electrons by ultra-low frequency (ULF) plasma waves. This can be achieved by improving models of ULF occurrence, including understanding the azimuthal variation of ULF waves and the underlying coupling to the solar wind [Horne *et al.*, 2013]. ULF waves are in the range 1 – 20 mHz, also known as the Pc 4-5 range following the classification in Jacobs *et al.* [1964]. Frequencies at the lower end of this band are most effective at radial transport, as there is more power on average at lower frequencies [Bentley *et al.*, 2018, Figure 1(a)]

47 and because lower frequencies can set up drift resonant diffusion [Elkington *et al.*, 1999,  
48 2003]. Hence it is important to examine the generation and propagation of the electromag-  
49 netic waves that drive this diffusion, and to construct a model of the resultant diffusion  
50 that will improve nowcasting and forecasting in the outer radiation belt. Current calcula-  
51 tions of radial diffusion coefficients can be constructed from the electromagnetic field in  
52 MHD models [Fei *et al.*, 2006] or from observations, either solely using in situ measure-  
53 ments [Lejosne *et al.*, 2013; Liu *et al.*, 2016] or by incorporating ground-based magnetic  
54 field measurements mapped up to the equatorial electric field [Ozeke *et al.*, 2009, 2012,  
55 2014]. In situ spacecraft provide more reliable measurements of the electromagnetic waves  
56 driving radial diffusion, but spacecraft coverage is sparse and has limited temporal cover-  
57 age. Ground-based magnetometer networks across the globe have produced many years of  
58 observations spanning multiple solar cycles [e.g. Rostoker *et al.*, 1995; Mann *et al.*, 2008;  
59 Tanskanen, 2009; Gjerloev, 2012]. By mapping these measurements of ULF waves up  
60 to the equatorial plane these networks can provide a long-term dataset with significantly  
61 better spatiotemporal coverage, allowing multiple simultaneous measurements at different  
62 locations and encompassing a large range of latitudes (and hence radial locations) and az-  
63 imuthal (or magnetic local time, MLT) sectors.

64 Existing models of radial diffusion coefficients are often parameterized by the geo-  
65 magnetic activity index  $Kp$  [Brautigam and Albert, 2000; Lejosne *et al.*, 2013; Ozeke *et al.*,  
66 2014; Ali *et al.*, 2016]. Individual radial diffusion models based on this parameterization  
67 can differ by orders of magnitude [Liu *et al.*, 2016; Ali *et al.*, 2016]. This makes it difficult  
68 to accurately capture radial diffusion in radiation belt models as the uncertainty in models  
69 is unquantified but could easily extend across orders of magnitude. While  $Kp$  is a proxy  
70 for geomagnetic activity, it is not directly related to processes driving ULF waves. Addi-  
71 tionally, as a three-hour averaged index, only forecasted  $Kp$  rather than real time  $Kp$  can  
72 be used for nowcasting or forecasting. The choice of parameters is an important part of  
73 constructing any kind of empirical model as the parameters chosen should have a clear  
74 physical basis in order to represent (and ultimately, to interpret) the physical phenomena  
75 underlying the observations. We propose a model based initially on solar wind parameters  
76 measured by spacecraft at the L1 Lagrange point, which has a lead time of around an hour  
77 [Richardson and Paularena, 1998; Weimer *et al.*, 2002; King and Papitashvili, 2005]. The  
78 use of solar wind parameters will also represent the external driving of magnetospheric

79 processes by the solar wind and will allow us to directly compare model results to our  
80 existing knowledge of those physical processes.

81 To address the large difference between existing radial diffusion models, we also  
82 propose a probabilistic model. In meteorology and climate modeling, probabilistic ap-  
83 proaches have met with considerable success in recent years as a method of improving  
84 models by accounting for uncertainty and variability in modelling, e.g. [Berner *et al.*,  
85 2017]. Probabilistic models produce a probability distribution as output instead of the sin-  
86 gle values produced by deterministic models, and can be used to quantify the uncertainty  
87 introduced by each model component. Model components or steps with larger uncertainty  
88 will therefore indicate areas where the model can be improved to better approximate the  
89 underlying physics, regardless of the physical process being approximated. Component un-  
90 certainties that should be quantified include uncertainty due to initial conditions, boundary  
91 conditions, the underlying physics model and (perhaps most importantly for this paper)  
92 due to natural internal variability in the system. Probabilistic methods provide a way to  
93 quantify variability that either exists naturally, or exists due to a parameterization that has  
94 yet to be optimised [Watt *et al.*, 2017].

95 The ultimate goal of this work is to construct a probabilistic model of diffusion co-  
96 efficients suitable for nowcasting and forecasting. In this article we focus our initial efforts  
97 on outlining a statistical model of ground-based power spectral density which can be used  
98 to probabilistically predict ULF wave power at the ground from solar wind observations  
99 across a range of frequencies, latitudes (i.e. L-shells) and azimuthal angles (magnetic local  
100 times, MLTs). We present the model concept and test it, but reserve comparison between  
101 the model and physics (i.e. ULF propagation and generation) for future work. In future  
102 this model can also be used to map along field lines to the equatorial plane in the magne-  
103 tosphere to calculate diffusion coefficients [Ozoke *et al.*, 2009].

104 In Section 2 we briefly review the relationship between ULF power spectral den-  
105 sity and radial diffusion coefficients. In Section 3 we present our initial solar-wind based,  
106 probabilistic model of ground-based ULF wave power which is available from the Read-  
107 ing Research Data Archive, Bentley [2019]. In Section 4 we define what qualities make  
108 a "good" parameterization and confirm that our model possesses these qualities. We also  
109 test the ability of our solar-wind based model to predict ULF wave power and compare it  
110 to a similar  $Kp$ -based model. In Section 5 we discuss other known sources of uncertainty

111 in the calculation of radial diffusion coefficients, in addition to the uncertainty introduced  
 112 by the underlying description ULF wave power addressed by our model. In Section 6 we  
 113 draw our conclusions and describe future work necessary to apply this initial ULF wave  
 114 model to the production of diffusion coefficients for radiation belt modeling.

## 115 2 ULF wave power and radial diffusion coefficients

116 The Fokker-Planck equation can be used in the outer radiation belt to determine the  
 117 evolution of a phase space distribution function  $\mathcal{F}$  due to diffusion from wave-particle  
 118 interactions, see e.g. *Schulz and Lanzerotti* [1974]. The most appropriate co-ordinate sys-  
 119 tem to use is based upon the set of three adiabatic invariants corresponding to quantities  
 120 conserved in periodic motions of particles trapped in Earth's magnetosphere - gyromotion  
 121 around a guiding centre, bounce motion along the magnetic field between mirror points  
 122 closer to the Earth and a drift around the Earth itself. We are particularly interested in the  
 123 case where a disturbance is on a timescale ( $\tau$ ) longer than gyromotion or the bounce pe-  
 124 riod of particles but shorter than or comparable to drift periods ( $\tau_{bounce} \ll \tau \lesssim \tau_{drift}$ ,  
 125 a range that extends from minutes to hours). This range of timescales corresponds to the  
 126 periods of ultra-low frequency waves and impulses such as changes in magnetopause lo-  
 127 cation, [*Southwood and Kivelson*, 1990; *Kepko et al.*, 2002; *McPherron*, 2005]. A dis-  
 128 turbance on such a timescale can then lead to a violation of the third adiabatic invariant  
 129 while the first two remain conserved. This can result in an increase of kinetic energy for  
 130 individual particles [see e.g. *Elkington et al.*, 1999; *Elkington*, 2013; *Roederer and Zhang*,  
 131 2014]. Additionally, the bulk transport of particles to drift contours closer to (or more  
 132 distant from) the Earth is particularly of interest when combined with particle sinks and  
 133 sources. For example, if there exists a source of particles far from the Earth and a sink at  
 134 low  $L$ -shell, this mechanism corresponds to a net transport of energy inwards. Similarly,  
 135 when there is a sink at the outer boundary of the magnetosphere (e.g. magnetopause shad-  
 136 owing, [*West Jun et al.*, 1972; *Loto'aniu et al.*, 2010; *Turner et al.*, 2012] ) radial diffusion  
 137 can result in a loss of energy. Hence radial diffusion contributes to the energization and  
 138 transport of particles in the outer radiation belt.

139 When considering only third-invariant diffusion, the diffusion equation reduces to

$$\frac{\partial \mathcal{F}}{\partial t} = L^{*2} \frac{\partial}{\partial L^*} \left[ \frac{1}{L^{*2}} D_{LL} \frac{\partial \mathcal{F}}{\partial L^*} \right] \quad (1)$$

140 [Schulz and Lanzerotti, 1974; Roederer and Zhang, 2014] with radial diffusion coeffi-  
 141 cient

$$D_{LL} = \frac{\langle(\Delta L^*)^2\rangle}{2\tau}, \quad (2)$$

142 where  $L^* = \frac{2\pi B_E R_E^2}{\phi}$  [Roederer and Zhang, 2014]. Hence  $L^*$  is related to the third adi-  
 143 abatic invariant, namely flux  $\phi$  through a drift contour, and is related to the equatorial  
 144 radius  $r_0$  of the corresponding drift contour in a dipole with no field perturbations. This  
 145 is clear using units of Earth radii, ( $L^* = r_0/R_E$ ). While the drift shell radius will change  
 146 once the dipole field is distorted, the  $L^*$  value will be conserved. Calculating the mean  
 147 square displacement in  $L^*$ ,  $(\Delta L^*)^2$ , reduces to an integral whose non-negligible terms use  
 148 the autocorrelation of electromagnetic field amplitudes [Fälthammar, 1965; Fälthammar,  
 149 1968; Fei et al., 2006; Lejosne et al., 2012]. The Fourier transform of the autocorrelation  
 150 function and power spectral density (PSD) are related via the Wiener-Khinchin theorem,  
 151 assuming a weakly stationary and stochastic signal. Hence PSD at each frequency is an  
 152 important component of  $D_{LL}$  [Fälthammar, 1965; Schulz and Lanzerotti, 1974; Fei et al.,  
 153 2006]. Typically, for radiation belt modeling  $(\Delta L^*)^2$  is estimated using electric and mag-  
 154 netic ultra-low frequency wave PSDs [Brautigam and Albert, 2000; Brautigam et al., 2005;  
 155 Fei et al., 2006; Ozeke et al., 2012, 2014; Liu et al., 2016; Ali et al., 2016].

156 This work focuses on constructing a statistical model of ULF PSDs that can quan-  
 157 tify the uncertainty passed forward into ULF wave derived radial diffusion coefficients.  
 158 However, there are multiple other sources of uncertainty in our diffusion coefficient cal-  
 159 culations which are reviewed in Section 5. These other sources can arise from physical  
 160 assumptions used in our formalism, from restrictions imposed by observation methods or  
 161 from statistical methods in creating models.

### 162 **3 Model construction**

163 In this section we discuss the method of construction of a statistical map of ground-  
 164 based ULF wave power, parameterized by physical properties that have been demonstrated  
 165 to causally correlate with power [Bentley et al., 2018] ("Paper 1"). Here, "causally corre-  
 166 lated properties" are properties whose correlation to ULF power cannot be attributed to  
 167 covariance with other solar wind parameters. The probabilistic model we outline can be  
 168 used to estimate the uncertainty in predictions of ULF wave PSDs. We will show that the



169 conditional probability distributions resulting from this parameterization can be approxi-  
 170 mated by a family of normal distributions whose mean and variance values make a "good"  
 171 parameterization. We discuss possible uses and testing of such a probabilistic model and  
 172 in future we also intend to use this to investigate the underlying physics of ULF genera-  
 173 tion and propagation.

174 To construct this statistical wave map we use the data as detailed in Paper 1; solar  
 175 wind observations from National Aeronautics and Space Administration/ Goddard Flight  
 176 Center's OMNI data set through OMNIWeb at <http://omniweb.gsfc.nasa.gov/> and ground-  
 177 based magnetic field measurements from the CANOPUS magnetometer chain in Canada  
 178 [Rostoker *et al.*, 1998] (now upgraded and expanded into the CARISMA array, [Mann  
 179 *et al.*, 2008]) to calculate PSD in hourly windows from 1990-2005 using the multitaper  
 180 method. This conserves the square of the signal in the time ( $t$ ) and frequency ( $f$ ) domain  
 181 as follows:

$$\sum_f PSD(f) = \Delta t \sum_t |x(t)|^2 = \int_{t=0}^T |x(t)|^2 dt \quad (3)$$

182 where  $x(t)$  is the detrended signal in the time domain and  $\Delta t$  the time resolution.

183 Previous work (Paper 1) has identified three near-instantaneous solar wind properties  
 184 that are causally correlated with ULF PSD: solar wind speed  $v_{sw}$ , interplanetary magnetic  
 185 field  $B_z < 0$  and summed perturbations in number density across 1.69 – 6.79 mHz,  $\delta N_p$ .  
 186 The method used to identify these properties accounts for skewed data distributions and  
 187 solar wind interparameter relationships by deconvolving the contribution of each individ-  
 188 ual solar wind parameter to ground ULF wave power from the relationship with other cor-  
 189 related solar wind parameters. Hence these solar wind properties are each directly related  
 190 to the occurrence of ULF wave power. In this paper we demonstrate the construction of  
 191 a parameterization using the three solar wind parameters above, with the expectation that  
 192 further parameters such as geomagnetic activity, magnetospheric plasma density distribu-  
 193 tion, substorms, time lags and history of the magnetosphere will be added as necessary in  
 194 future. In this work we choose to use  $var(N_p)$  in place of  $\delta N_p$  as it is equivalent in the  
 195 analysis method of Paper 1 but is simpler to use.

**Table 1.** Parameters used to discretely partition model

Parameter	Values	num. values
Radial L-shell (Station latitude)	Four stations FCHU, GILL, ISLL, PINA ( $L \sim 7.94, 6.51, 5.40, 4.21$ )	4
Frequency	0.83 – 20 mHz	69
Azimuthal angle (MLT)	Dawn, noon dusk and midnight (3-9, 9-15, 15-21 and 21-3 MLT)	4
$B_z = 0$ threshold	$B_z > 0$ and $B_z < 0$	2

These parameters define the separate partitions. Solar wind properties  $v_{sw}$ ,  $B_z < 0$ ,  $var(Np)$  are used in each partition to parameterize the power observed.

197

### 3.1 Partitions of the magnetosphere

198

199

200

201

202

203

204

205

206

207

208

209

210

211

212

213

214

215

216

217

To capture the changing behavior of ULF waves in different regions of the magnetosphere, we define a set of nested bins. We call the magnetospheric bins "partitions", which depend on frequency, azimuthal angle (i.e. magnetic local time) and radial location (i.e. L-shell, defined by station latitude). These are reviewed in Table 1. The parameterization using three solar wind properties is performed separately in each partition, so that our final empirical model is dependent on the solar wind, the region of the magnetosphere, and ULF frequency. For the remainder of this article, "bins" will solely refer to the nested solar wind parameter bins nested in each partition. We choose to cover frequencies from 0.8 to 20 mHz. Lower frequencies contain the most power but as the power tends to drop off gradually with frequency [Bentley *et al.*, 2018, Figure 1(a)], we also include higher frequencies in order to examine their contribution. The dataset is already discretised by radial location and frequency (due to the use of different ground magnetometer stations and our PSD calculation) and we subdivide the data further into four MLT sectors centred at dawn, noon, dusk and midnight. Use of four sectors allows us to resolve azimuthal variations while retaining enough data to construct a parameterization. In addition, we split the data at  $B_z = 0$  as Paper 1 indicates that the physical processes either driving or propagating ULF waves differs for  $B_z > 0$  and  $B_z < 0$ . This will aid future analysis of the physics. The full L-shell ranges corresponding to the four magnetometer stations FCHU, GILL, ISLL and PINA over this time period can be found in Table 1 of Rae *et al.* [2012].

218

219

Therefore in total we have  $4 \times 69 \times 4 \times 2 = 2208$  partitions. In each of these, we parameterise ULF wave power using  $v_{sw}$ ,  $B_z < 0$  and  $var(Np)$  bins. In this paper we present

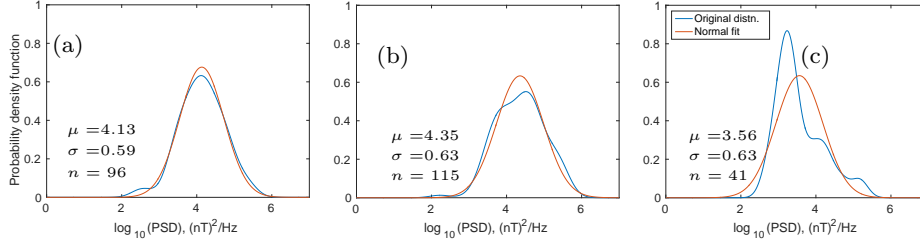
220 and test the results of the ground based geomagnetic north-south component in order to  
 221 validate our approach. The east-west component is also included in the dataset. Together,  
 222 these comprise the magnetospheric toroidal and poloidal modes [Elkington, 2013] plus  
 223 some mixing. The final, perpendicular component represents the compressional mode and  
 224 is not included.

### 225 3.2 Parameterization in each partition

226 The model in each partition is constructed by binning ground-based ULF wave power  
 227 by the corresponding solar wind properties. We remove the 0.1% most extreme solar wind  
 228 values to improve data resolution, (i.e. the lowest and highest 0.05% values). This results  
 229 in a parameter space where the ends bins are not unnecessarily large and empty. The rel-  
 230 evant ranges are velocity: 282 to 783 km s<sup>-1</sup>, variance of proton number density: 0.0038  
 231 to 42.814 cm<sup>-3</sup> and  $B_z$ : -12.3 to 11.5 nT. From this point onwards we use  $\log_{10}(\text{var}(N_p))$   
 232 instead of  $\text{var}(N_p)$  in order to work with linear scales in our parameterization. Bins are  
 233 equally spaced on this linear scale and are the same in each partition.

234 In any one partition (i.e. for one station, MLT sector, frequency and for  $B_z < 0$  or  
 235  $> 0$ ) we determine conditional probability distributions of ULF wave power given obser-  
 236 vations of solar wind properties  $v_{sw}$ ,  $\log_{10}(\text{var}(N_p))$  and  $B_z$ . We bin observed power into  
 237 a 10x10x5 grid, and examine the distribution of  $\log_{10}(PSD)$  in each bin. Since we split at  
 238  $B_z = 0$ , the  $B_z$  dimension only has 5 bins instead of 10. For each partition, this creates  
 239 a 3d look-up table of probability distributions that are parameterized by the solar wind  
 240 observations. These are therefore conditional probability distributions as they express the  
 241 probability distribution given a particular set of solar wind properties.

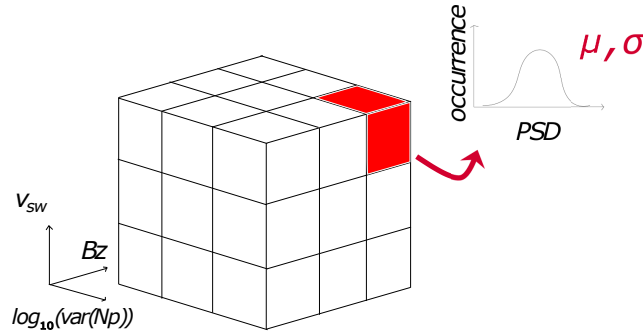
242 The distribution of  $\log_{10}(PSD)$  in each bin is approximated with a normal distri-  
 243 bution, by fitting a normal to the log-power observed in each bin containing at least 10  
 244 points. While the majority of bins contain distributions of log-power that are technically  
 245 statistically distinct from normal distributions, they are nonetheless reasonable approxi-  
 246 mations. In Figure 1 we show example distributions from three bins in a single partition;  
 247 a probability distribution that is highly likely to be drawn from a normal distribution as  
 248 measured using a chi-square goodness of fit test (panel (a)) and two others that are far less  
 249 likely (b) and highly unlikely (c). While all three may not be exactly normally distributed,  
 250 this makes a reasonable approximation, with the arguable exception of (c). However, even



257 **Figure 1.** The original and normal (fitted) distributions of logpower in three example bins from the GILL  
 258 station at  $L \sim 6.6R_E$ , 3.33 mHz, with  $B_z < 0$  in the noon sector; the three distributions most likely (a),  
 259 highly unlikely (b) and least likely (c) to be drawn from a normal distribution, with chi-square p-values of  
 260  $p = 0.95, 0.13, 0.01$  respectively. Bin (a) is centred at  $v_{sw} = 558 \text{ km s}^{-1}$ ,  $\log_{10}(\text{var}(Np)) = -0.059 \text{ cm}^{-3}$ ,  
 261  $B_z = -1.23 \text{ nT}$ . (b) is centred at  $608 \text{ km s}^{-1}$ ,  $-0.999 \text{ cm}^{-3}$ ,  $-1.23 \text{ nT}$  and (c) is centred at  $407 \text{ km s}^{-1}$ ,  $0.620$   
 262  $\text{cm}^{-3}$  and  $-1.23 \text{ nT}$ . For each bin, the mean  $\mu$  and standard deviation  $\sigma$  of the distribution of the  $n$  points in  
 263 that bin are shown.

251 for this poor fit, a normal approximation is preferable to having nothing in this bin. The  
 252 poor fit of 1 (c) indicates how uncertainty can enter PSD prediction when underlying ap-  
 253 proximations (here, the lognormal assumption) are less valid. Examining where these fits  
 254 are good approximations is an example of the future analysis that can be done to investi-  
 255 gate the physics, as the type of distribution may provide insight into the underlying physi-  
 256 cal processes.

264 Constructing a distribution for each bin in a given partition provides multiple bene-  
 265 fits compared to simply taking the mean or median; firstly, if we choose to use the mean  
 266 or median in future we retain information about the range and variance. Secondly, we are  
 267 able to then use these distributions for probabilistic forecasting. We note that as the dis-  
 268 tribution in each bin describes the occurrence of ULF wave PSD depending on the solar  
 269 wind conditions, this is a set of conditional probability distribution functions, which al-  
 270 lows us to explore the physics of ULF occurrence in new ways. By approximating these  
 271 probability distributions as lognormals we can use this information relatively cheaply, as  
 272 for every single bin in a given partition we need only store the mean and variance of each  
 273 normal distribution of log-power rather than the entire distribution.

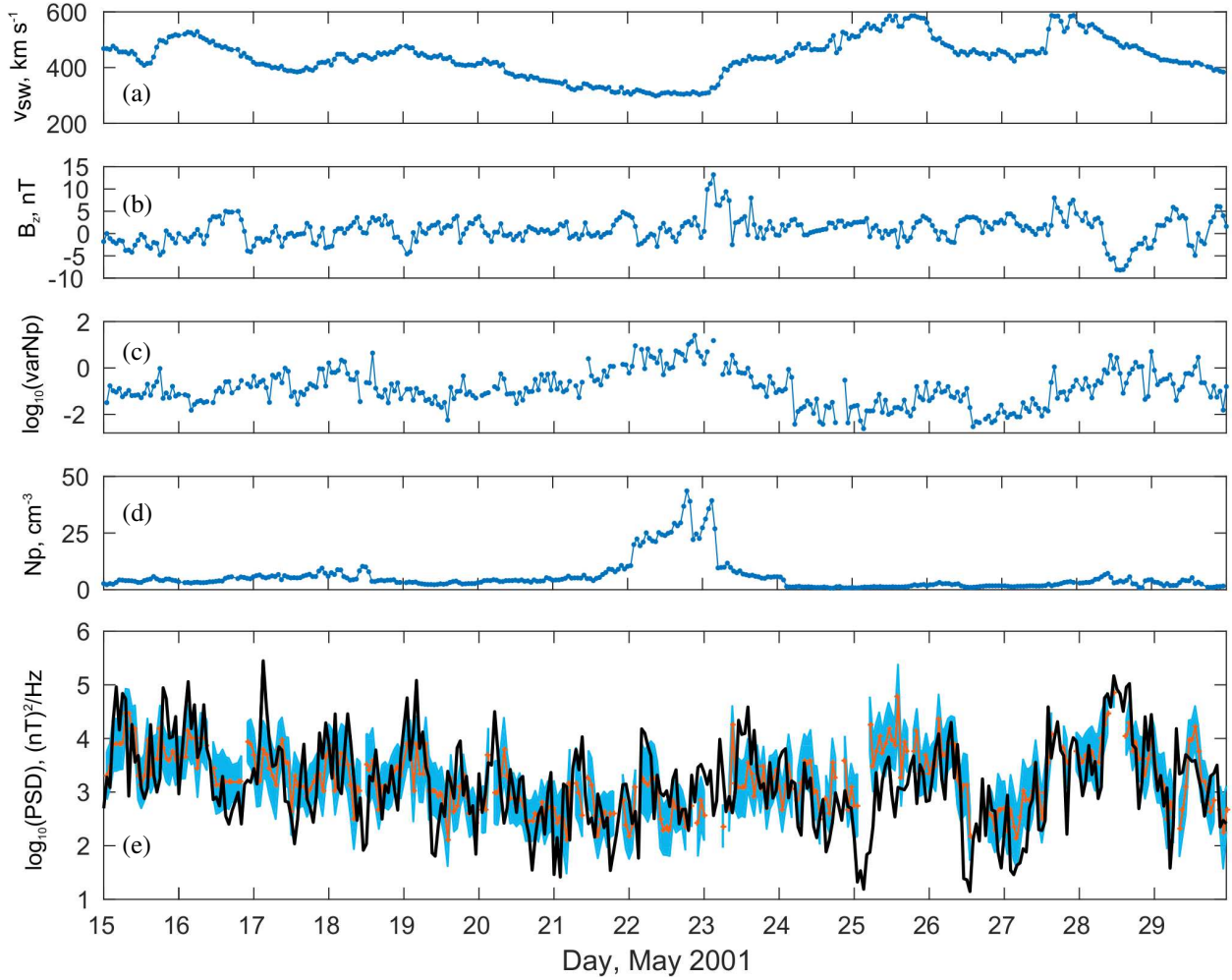


275 **Figure 2.** A visualization of our parameterization for each station, magnetic local time sector and frequency  
 276 partition. Using a 3-d grid with solar wind speed, variance of proton number density and interplanetary  
 277 magnetic field axes, ground-measured ULF wave log-power is binned and the corresponding probability dis-  
 278 tributions (a family of normal distributions) are used to model the power. We use 10, 10 and 5 bins for each  
 279 solar wind parameter respectively in the model.

### 274 3.3 Example: using this model

280 We have produced a series of look-up tables which, for each partition (station/freq/MLT/Bz  
 281  $<$  or  $>$  0), contain a family of normal distributions parameterized by the near-instantaneous  
 282 solar wind properties. Figure 2 illustrates this; we can use the bins nested in each partition  
 283 to look up the distribution function of ULF PSD values for a given solar wind speed, vari-  
 284 ance of proton number density and  $B_z$  observed in the solar wind (i.e. conditional prob-  
 285 ability distribution functions). Hence at each point in time this model can be used in two  
 286 ways; given the solar wind observations, we can look up the corresponding conditional  
 287 probability distribution and either use the expectation value (i.e. the mean) of the distribu-  
 288 tion, or sample the entire distribution. Sampling will randomly obtain PSD values drawn  
 289 from the probability distribution in a given bin. With many such samples, the distribution  
 290 of our predicted values will converge towards the original distribution in that bin. In this  
 291 way a time series of reproduced power can then be built up an hour at a time, either deter-  
 292 ministically (i.e. using the mean) or stochastically (by sampling).

301 An example reproduced hourly time series is shown in Figure 3 where we show the  
 302 solar wind speed  $v_{sw}$ , variance in number density  $\log_{10}(\text{var}(Np))$ ,  $B_z$  and the original and  
 303 reproduced log-power measured at GILL station, 3.33 mHz, for two weeks in May 2001.  
 304 We also show the number density  $Np$  for reference. The reproduced power shown in (e)  
 305 can be found by using the mean values in each look-up table (orange) or by sampling. For



293 **Figure 3.** Using instantaneous solar wind speed  $v_{sw}$  (a), southward interplanetary magnetic  $B_z$  (b) and  
 294 variance in proton number density  $\log_{10}(\text{var}(Np))$  (c), the power spectral density observed across all MLT  
 295 sectors at a single station and frequency (GILL, 3.33 mHz) can be reproduced using a family of normal prob-  
 296 ability distributions parameterized by solar wind properties. Panel (e) shows the original power time series  
 297 (black) and power reproduced using our model, either by taking the mean of the probability distribution given  
 298 the observed solar wind values (orange) or by sampling from that distribution multiple times (the interquartile  
 299 range of 2000 samples is shown in blue). Panel (d) shows the proton number density in the solar wind for  
 300 reference.

306 the sampling method, 2000 time series were constructed and for each hour in Figure 3 the  
307 blue sleeve indicates the the interquartile range of samples taken. This time period was  
308 chosen for the variety of solar wind speed conditions; however, the few gaps in our re-  
309 production also highlight some areas of our model that can be improved. These gaps are  
310 primarily due to data gaps in the solar wind observations in variance of number density  
311 (absent  $\sim 15\%$  of the time from 1990-2005 when OMNI data is supplied for  $v_{sw}, Bz$ ) and  
312 also due to too few observations in the more extreme bins, preventing us from determining  
313 the underlying probability distribution. We anticipate that these will be addressed using  
314 additional solar wind observations and/or  $Np$  correlations for the former, and additional  
315 years of data and/or extrapolations for the latter. More simply, approximations could be  
316 made using only  $v_{sw}$  and  $Bz$ . In Figure 3(e) it can be seen that the observed and repro-  
317 duced log-power roughly follow each other. Overall the model appears to have performed  
318 exceedingly well given that it depends primarily on the instantaneous contribution of three  
319 solar wind properties, and includes no time lags or properties internal to the magne-  
320 sphere. There appears to be a diurnal variation which is captured reasonably well by the  
321 four MLT sectors used here; the relative contribution of the solar wind parameters and  
322 MLT sectors to the PSD observed throughout the magnetosphere will be considered in fu-  
323 ture work. However, first we must verify that our model is a good approximation to the  
324 original PSD observations. We discuss different metrics for testing this model below.

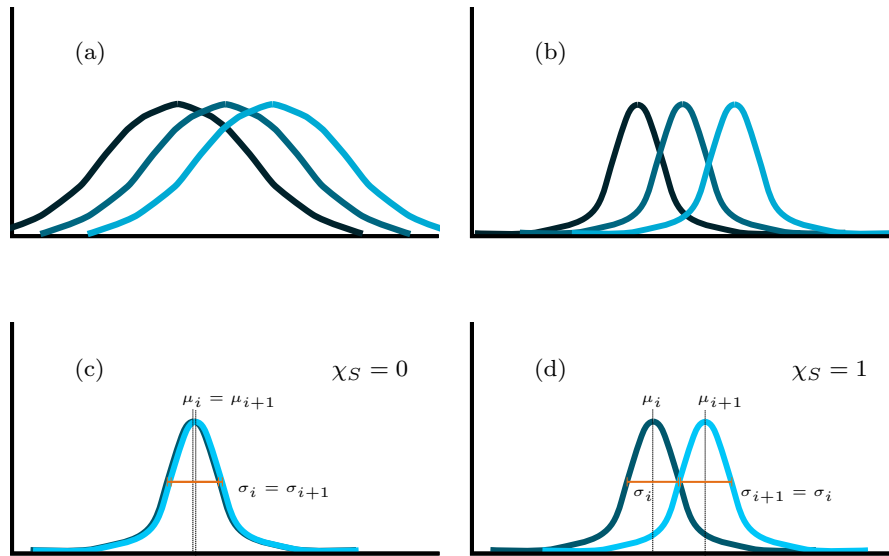
## 325 **4 Testing the model**

326 While the ability to reproduce observed phenomena is an important test of a model,  
327 other model qualities determine whether it is fit for purpose and whether it produces sta-  
328 tistically significant results. We discuss all these qualities first, before building metrics in  
329 Section 4.2 to measure the ability of our model to reproduce ULF wave power observa-  
330 tions and comparing to a similar  $Kp$ -based model in Section 4.3.

### 331 **4.1 A "good" parameterization**

332 We use the following criteria to define a good parameterization, in no particular or-  
333 der:

- 334 1. The parameterization reproduces behavior well, as measured by a relevant metric.



342 **Figure 4.** (a)-(b) An illustration of two sets of three normal distributions, which have the same three mean  
 343 values but a larger (a) and smaller (b) variance. We would consider (b) a better parameterization as there is  
 344 considerably more overlap between neighboring probability distributions in (a). (c) and (d) show the dis-  
 345 tribution overlap corresponding to separation proxy values of zero and one respectively, when the standard  
 346 deviations of each distribution are roughly the same.

- 347 2. Parameters chosen are significantly related to changes in power spectral density, i.e
- 348 the probability distribution of power values in neighboring bins are distinct. Vari-
- 349 ance is minimised while the mean values are much larger and vary more.
- 350 3. Parameters are physically motivated and we can interpret their impact
- 351 4. The parameterization can be used for nowcasting and forecasting
- 352 5. Excess parameters are excluded to avoid overfitting, as models with larger degrees
- 353 of freedom are less statistically significant.

347 The ability of our model to reproduce observed PSD values is examined in Section  
 348 4.2. The importance of the second criterion is illustrated in Figure 4(a) and (b); the larger  
 349 the variance in each bin, the more likely that neighboring probability distributions overlap.  
 350 This is a consequence of our finite amount of data, which in turn can only be binned by  
 351 a finite number of parameters. With infinite data, considerable overlap would be fine and  
 352 we could bin by all physically motivated parameters. Instead, when we can only use a  
 353 finite number of parameters a clear evolution of PSD distribution across neighbouring bins  
 354 suggests that the parameters chosen are significantly related to changes in PSD. Numerous



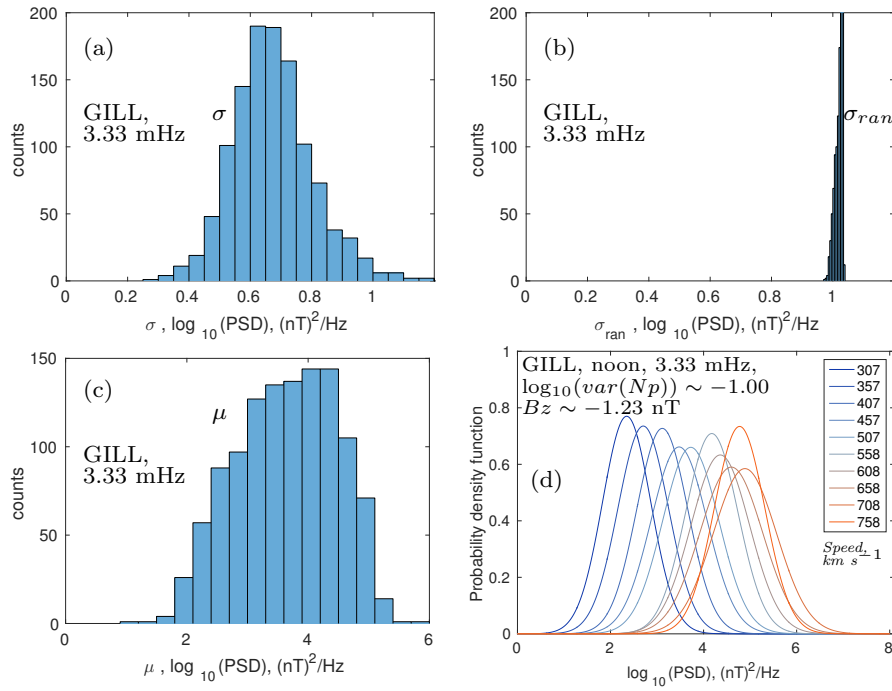
355 overlap coefficients exist to examine the relationship between two normal distributions,  
 356 but we can define a simple metric here specifically to quantify how this overlap affects  
 357 the quality of our parameterization. This metric is particularly suitable as the standard  
 358 deviation of all our bins are so similar (discussed below). We use the ratio of the standard  
 359 deviation in each bin to the difference in mean values; for two neighboring bins  $b_i, b_{i+1}$   
 360 this quantity is then the separation proxy

$$\chi_S = \frac{\|\mu_i - \mu_{i+1}\|}{\langle \sigma_{i,i+1} \rangle} \quad (4)$$

361 which (as illustrated in Figure 4 (c) and (d)) will be zero for two completely over-  
 362 lapping distributions but will be equal to 1 for two distributions with equal standard de-  
 363 viations, where the point of overlap is exactly one standard deviation of either mean. The  
 364 median values of this separation proxy between all neighboring bins for GILL, 3.33 mHz,  
 365 noon,  $Bz < 0$  is 0.5 for probability distributions along the speed axis, 0.28 along  $\log_{10}(\text{var}(Np))$   
 366 and 0.37 along  $Bz$ . For GILL, 3.33 mHz, noon,  $Bz > 0$  these values are 0.6, 0.29 and  
 367 0.25 respectively. The magnitude of these values corresponds to the order of dominant  
 368 contributing parameters  $v_{sw}, Bz < 0$  and  $\text{var}(Np)$  as expected and indicate that in fu-  
 369 ture such a measure can be used to investigate where the solar wind parameters contribute  
 370 meaningfully to changes in ULF power.

371 This separation proxy  $\chi_S$  is very similar to the well established effect size measure  
 372 Cohen's  $d$  [Cohen, 1988]. Instead of standardising the two mean values by the average  
 373 standard deviation  $\langle \sigma_{i,i+1} \rangle$ , Cohen's  $d$  standardises by the "pooled" standard deviation  
 374 which weights by the number of points in each distribution. This is unnecessary here as  
 375 the normal distributions are already known to be approximations, and the uncertainty aris-  
 376 ing from that approximation should be decoupled from our separation proxy and investi-  
 377 gated separately. However, we note that in the case where  $\sigma_i = \sigma_{i+1}$ , much of the existing  
 378 literature on interpreting Cohen's  $d$  can still be applied here.

386 Indeed, the separation proxy  $\chi_S$  is most meaningful where the standard deviations  
 387 of all distributions are roughly the same, hence a more detailed comparison of mean and  
 388 standard deviation ( $\mu, \sigma$ ) values is made for all bins at GILL, 3.33 mHz in Figure 5. Fig-  
 389 ure 5(a) shows the distribution of all  $\sigma$  values, which is clustered around  $\sim 0.7$ . This  
 390 can be compared to Figure 5(b), which shows the  $\sigma$  of normal distributions fitted to the  
 391 same number of power values which were randomly selected from the original distribu-



379 **Figure 5.** (a) the standard deviation ( $\sigma$ ) values of the normal fitted probability distributions for all bins  
 380 at GILL, 3.33 mHz. (b) the  $\sigma$  values of normal distributions fitted to bins of equal size as those in (a), but  
 381 randomly sampled from the original distribution. (c) the mean ( $\mu$ ) values of the normal probability distribu-  
 382 tions, corresponding to those in (a). There is less variance in each probability distribution when binning by  
 383 three solar wind parameters than in equivalent randomly sampled distributions, and this variance is small and  
 384 consistent relative to the range of mean values. (d) An example of the variation of probability distributions  
 385 with speed in a constant  $Bz, \text{var}(Np)$  bin in a single partition.

392 tion rather than using our binning technique. (This was run 1000 times). As the variance  
 393 is smaller for our parameterization, our model is outperforming randomly selected dis-  
 394 tributions. Figure 5(c) shows the  $\mu$  values for GILL, 3.33 mHz, corresponding to the  $\sigma$   
 395 shown in (a). This range of mean values indicates that the mean power (i.e. PSD, not  
 396  $\log_{10}(PSD)$ ) varies over several orders of magnitude while the variance of each distribu-  
 397 tion is about an order of magnitude for each bin. Hence the family of probability distribu-  
 398 tions we use is better than randomly selected distributions as the variance is smaller, and  
 399 the variance/mean ratio is such that changes in the solar wind parameters correspond to  
 400 the probability distribution shifting up and down the power axis without changing shape.  
 401 An example of this can be seen in Figure 5(d); the probability distributions associated  
 402 with different solar wind speed values for constant  $B_z, var(Np)$  bin is shown for GILL,  
 403 3.33 mHz in the noon sector,  $B_z < 0$ . For lower solar wind speeds the distributions are  
 404 distinct, while at higher speeds they overlap. Future improvements of this parameterization  
 405 could involve identifying where such distributions should be merged using  $\chi_S$ , while iden-  
 406 tifying what this corresponds to physically is one example of the future work that can be  
 407 done to understand the underlying physics using this probabilistic model.

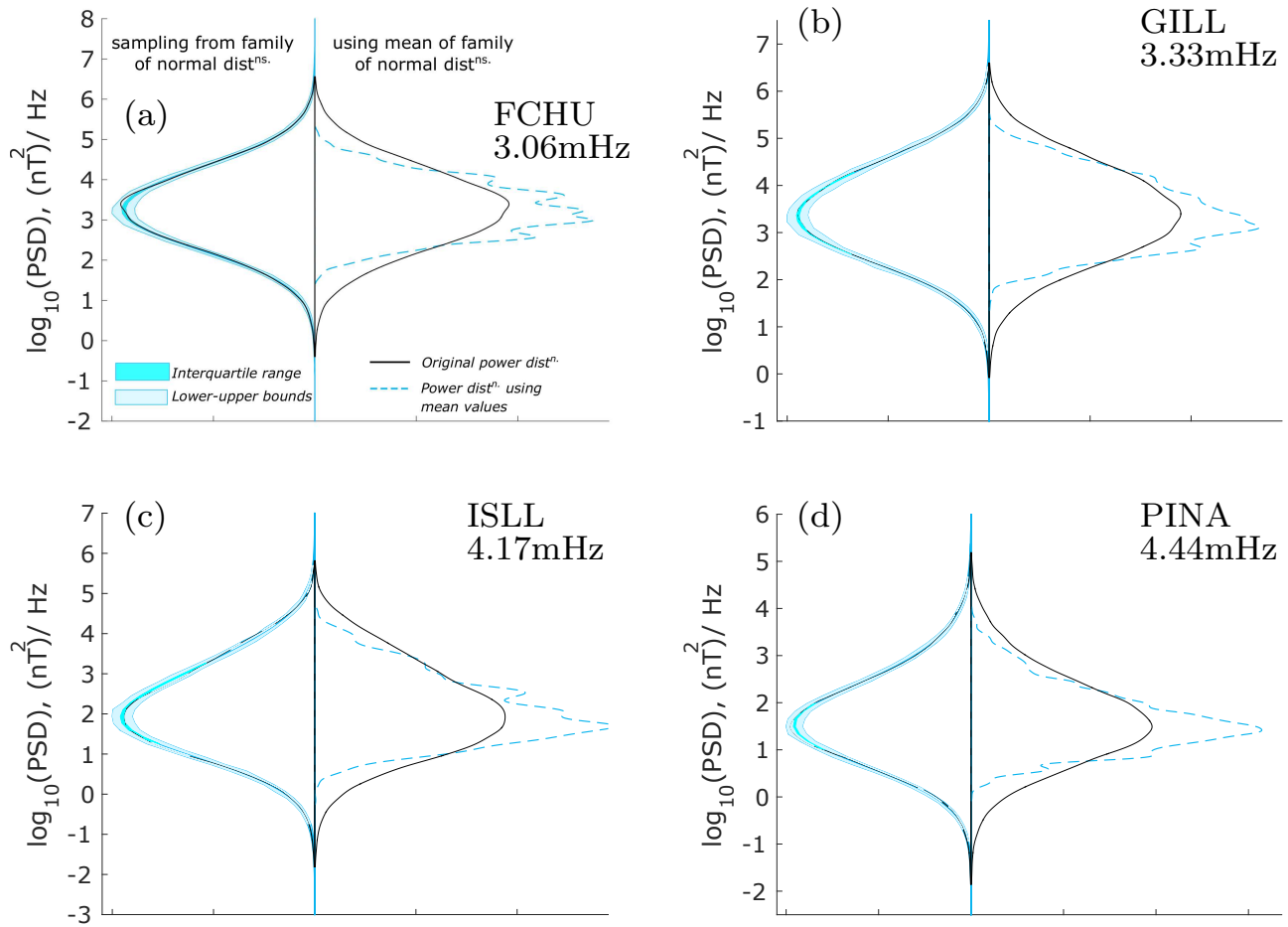
408 Criteria 3 and 4 reflect the intention that our model be capable of investigating ex-  
 409 isting physics and, eventually, to be capable of forecasting. For a model parameterizing  
 410 radial diffusion coefficients, the chosen parameters should also be clearly and significantly  
 411 related to changes in the diffusion coefficients. The solar wind parameters used in this  
 412 model were selected as they have been shown to be causally correlated to ground ULF  
 413 wave power; a review of their physical interpretation can be found in Paper 1. As they are  
 414 drawn from solar wind observations they can be used for nowcasting and forecasting. We  
 415 have attempted to reduce the degrees of freedom by only using causally correlated solar  
 416 wind parameters, and by using a long time period, which makes overfitting on the five pa-  
 417 rameters here ( $L, MLT, v_{sw}, B_z, var(Np)$ ) unlikely.

## 418 **4.2 Ability to predict ULF wave power**

419 We anticipate that our model will be put to two main uses: calculating the total  
 420 power distribution over an extended event or predicting the power for each hour in a time  
 421 series. For example, the total distribution method will be useful for long timescale recon-  
 422 structions where it is important to reproduce signal properties that include the overall dis-  
 423 tribution, while the time series will be useful for forecasting. Both outputs may be useful

424 to case studies of individual events. Therefore we examine the efficacy of this model using  
425 two tests. The first (a series of violin plots) compares the total distribution of log-power  
426 from the original observed log-power to the distribution of log-power reproduced from  
427 our model. The second test (forecasting skill) examines the ability to predict power in the  
428 oncoming hour compared to a reference model. Both these tests are completed first on  
429 sample partitions of the entire 15 years of original data and on a small set of CARISMA  
430 data from Jan-Mar 2015, i.e. we test our model on both the training data and on data out-  
431 side the training window. Customarily such testing is not done on training data, however  
432 the size of the dataset compared to the few parameters we have used suggests that this is a  
433 reasonable test.

434 We use vertically plotted probability distribution functions (violin plots) in Figure  
435 6 to compare original and reproduced probability distributions of PSD over an extended  
436 time. Here we have chosen four representative combinations of station and frequency; the  
437 frequency for each station is the average eigenfrequency over all MLT as calculated by the  
438 cross-phase technique [Waters *et al.*, 1991; Sandhu *et al.*, 2018] over several years. Hence  
439 this is a stricter test than choosing consistently "quiet" frequencies for each station. For  
440 each combination the total original power distribution (black) is compared to reproduced  
441 power using the mean of each probability distribution (right, blue) and to sampling from  
442 the probability distributions (left, blue). As the original distribution falls roughly between  
443 the interquartile range when using the sampling method, but is clearly very far off for the  
444 means method, this suggests that a sampling method is suitable for obtaining the power  
445 distribution over an extended event while the mean is not. Interestingly PINA and FCHU  
446 appear to have the worst fits, which may be due to the changing plasmopause and magne-  
447 topause locations crossing these respective stations. This is an example of the latitude and  
448 MLT dependent physics we intend to explore in future. Unfortunately it is very difficult to  
449 statistically quantify the ability to reproduce these distributions without overly favoring ei-  
450 ther the centre of the distribution or the tails; we have been unable to find a suitable met-  
451 ric. Existing measures designed to measure the similarity of two distributions found our  
452 sampled reproductions to be either all very good or all very poor. Therefore future study  
453 is necessary to identify a metric that accurately reflects our ability to reproduce the phys-  
454 ical distributions and that can be used as a tool to improve our model by distinguishing  
455 where fits are good or bad.



456 **Figure 6.** Violin plots showing the probability distribution of power over the original fifteen years of data,  
 457 compared to reproduced distributions of power using the two methods possible with our model. For each hour  
 458 the model defines a probability distribution of power which is dependent on solar wind conditions; this is used  
 459 to reproduce the original fifteen-year distribution. The left hand side of each violin compares the original  
 460 total power distribution to the reproduced distribution found by sampling from the conditional probability  
 461 distribution of power for each hour, while the right hand side compares to taking the mean value of the condi-  
 462 tional probability distribution for each hour. Black lines indicate the original distribution while the reproduced  
 463 values are indicated by a dashed blue line (mean values), a blue region (interquartile range of 2000 samples)  
 464 and light blue region (upper and lower bounds from sampling). This is shown for four combinations of station  
 465 and frequency. Violins are all scaled so that the area under the original and reproduced distributions are equal  
 466 to 1.

467 Forecasting skill is a simple measure that can be used to compare the ability of two  
 468 methods to predict a time series. In space physics, it has previously been used to test solar  
 469 wind predictions, e.g. *Owens et al.* [2013]. It is calculated as follows:

$$Skill = 100 \left( 1 - \frac{MSE_{model}}{MSE_{ref}} \right) \quad (5)$$

470 using the mean square error (MSE) between each model and the observed values.  
 471 Forecast skill scores can range from  $-\infty$  to 100 and positive values indicate that the tested  
 472 model is better than the reference model. We compare both mean and sampling methods  
 473 of applying our model and two "persistence" models to a random model sampling from  
 474 the entire original distribution of power, as per *Owens et al.* [2013]. The two persistence  
 475 models assume that the power we see in the next hour will be the same as that observed  
 476 24 hours ago and 1 hour ago respectively. Calculating forecasting skill is relatively simple  
 477 using the means or persistence method as the reproduced time series is always the same.  
 478 To calculate forecasting skill for random and sampling methods, 2000 time series were  
 479 constructed by sampling from either the random or appropriate normal distributions. The  
 480 forecasting skill was calculated for each of these time series and the median forecasting  
 481 skill of these 2000 runs taken. Results of this are shown in Table 2.

486 For all four examples, both means and sampling methods of using our model were  
 487 better than randomly sampling, as expected. However, both methods were also superior to  
 488 assuming 24 hour persistence and using the expected (mean) value from our look-up ta-  
 489 bles is a better predictor of power than assuming that power continues from the previous  
 490 hour. For example, at FCHU 3.06 mHz, all four models tested are better than the base-  
 491 line "random" model as they all have positive values. With the highest forecasting skill  
 492 score of 74.6, using the mean values of each parameterized probability distribution outper-  
 493 forms all other models, followed by 1h persistence with a score of 69.1. Sampling from  
 494 the probability distributions lags behind this with a skill score of 48.7 and 24h persistence  
 495 performs least well with a score of 34.9. To confirm that this ranking is not frequency de-  
 496 pendent, we have also calculated forecasting skill across 1990-2005 for every frequency at  
 497 a single station (GILL) using a smaller number of runs, shown in Figure 7. Across all fre-  
 498 quencies, the ranking of models compared to a random reference model remains the same.  
 499 Hence using the mean value is the best method for reproducing a time series whereas the  
 500 sampling method is outperformed by 1h persistence. However, it should be recalled that

**Table 2.** Forecasting skill at selected stations and frequencies

Partition Tested	Model skill score vs random reference model			
	24h persistence	1h persistence	Model (sampled)	Model (means only)
FCHU, 3.06 mHz	34.9	69.1	48.7	74.6
GILL, 3.33 mHz	38.0	74.1	55.6	78.0
ISLL, 4.17 mHz	37.6	76.2	56.5	78.4
PINA, 4.44 mHz	35.3	72.7	54.8	77.6

Forecasting skill scores for four stations and frequencies, testing the ability of the solar wind parameterized model to reproduce the original fifteen years of data. The baseline reference model used is a "random" model, where power is sampled from the original total distribution of the given partition. Simple 24-hour and 1-hour "persistence" models are tested against this baseline (i.e. assuming power in the oncoming hour is the same as the previous day or hour) in addition to the solar wind-parameterized model. The probability distributions predicted for each hour by the solar wind model were either sampled or the mean value was taken to construct each fifteen year time series. Where sampling methods were used, 2000 time series were made and the forecast skill calculated for each one; the median is shown here.

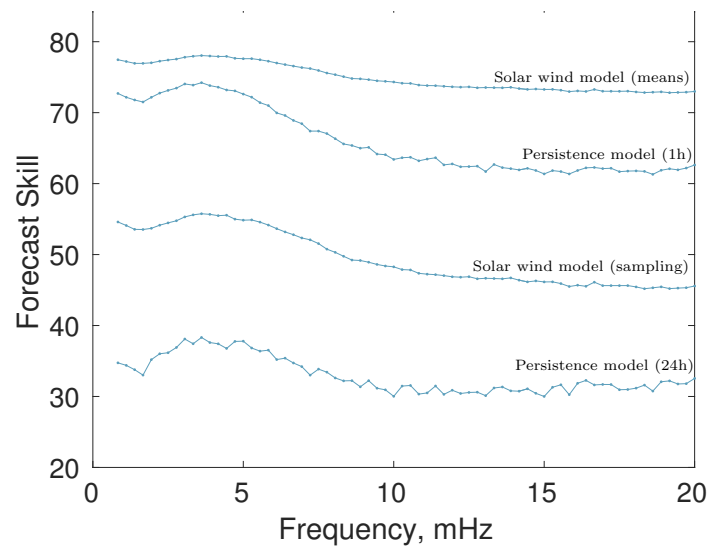
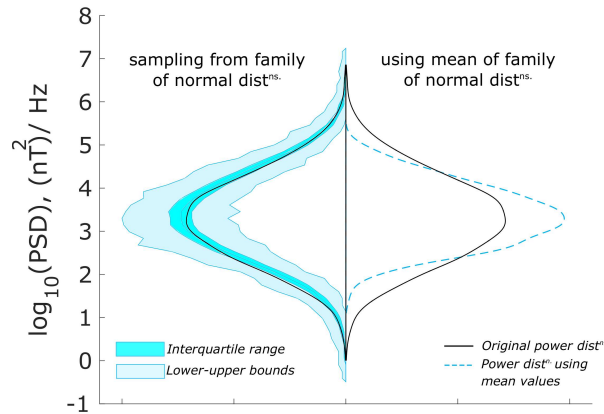


**Figure 7.** Forecasting skill at all frequencies for GILL, 1990-2005, where models are compared to a random reference model. Where any kind of sampling was used (i.e. random and solar wind model sampling), 500 runs were taken. The ranking of model types is consistent across all frequencies.



Model skill score vs random reference model			
24h persistence	1h persistence	Model (sampled)	Model (means only)
37.3	73.8	53.9	76.7

504 **Figure 8.** Testing the ability of a solar wind-parameterised model to predict ground-based power not in our  
 505 training set, across January-March 2015, GILL, 3.33mHz. The violin plot compares both the sampled and  
 506 mean-value methods against the original total power distribution over an extended time period (as in Figure  
 507 6) and the forecasting skill tests the ability of models to reproduce a time series. Here we compare the perfor-  
 508 mance of two persistence models and our solar wind-parameterised model (using both sampling and the mean  
 509 methods) to a baseline "random" model, as described in Table 2. Results are very similar to the tests carried  
 510 out on the training data; the sampling method reproduces the power distribution well (as the original power  
 511 lies within the interquartile range of reproductions) while the mean value predicts the oncoming hour best.

501 the sampling method outperformed the mean method for reproducing the total distribution  
 502 (as tested using violin plots in Figure 6). Therefore different construction methods should  
 503 be used depending on the desired output.

512 Similarly, we test these methods for 3.33 mHz at GILL using CARISMA data for  
 513 Jan-Mar 2015 in Figure 8. Again, the sampling method is best for reproducing the total  
 514 power distribution over these two months and the mean method is superior at predicting  
 515 the power in individual hours. Note that while the sleeve between the upper and lower  
 516 bound in the violin plot of Figure 8 is wider than in Figure 6, this is a slightly misleading  
 517 visualisation artefact due to plotting less populated distributions, as the CARISMA data  
 518 is considerably shorter. It is more important to note that the original power distribution  
 519 shown in black still lies within the interquartile range of our samples. This emphasises the



520 need for a metric that quantifies the ability of the model to reproduce total power distribu-  
 521 tions, rather than relying on visualisations.

### 522 **4.3 Comment on other possible parameters**

523 The parameters used so far correspond to three near-instantaneous solar wind prop-  
 524 erties and the radial and azimuthal location in the magnetosphere. Therefore there is no  
 525 history of the solar wind or the magnetosphere, including the persistence of existing ULF  
 526 waves. The method presented in this paper does not represent internal properties such as  
 527 substorm activity or magnetospheric plasma density; therefore our current distributions av-  
 528 erage over all internal configurations. This is likely to contribute to the variance in each  
 529 distribution and requires further study. While no internal parameters or geomagnetic in-  
 530 dices are included, we compare our results to a  $Kp$  based model below. Finally, our se-  
 531 lection of parameters includes no long-term dependencies, such as seasonal or solar cycle  
 532 variations. It has long been understood that ULF wave activity varies with solar activity  
 533 phase [Saito, 1969; Murphy *et al.*, 2011]. An underlying assumption of this work is that  
 534 such effects can be characterised by the changing solar wind parameters  $v_{sw}, Bz, var(Np)$ ,  
 535 rather than representing this changed solar output indirectly using a parameter such as  
 536 F10.7. As the magnetospheric mass density also varies over a solar cycle, once internal  
 537 properties have been included the ability of our chosen parameters to represent ULF wave  
 538 power changes across a solar cycle could be compared to F10.7. More sophisticated meth-  
 539 ods will be necessary to add further parameters as we cannot further reduce the number of  
 540 data points in each bin.

### 541 **4.4 Comparison to $Kp$ -based models**

542 Existing models of radial diffusion coefficients and ULF wave PSD use  $Kp$ . We  
 543 cannot compare directly to the values predicted by the  $Kp$ -parameterised ground-based  
 544 empirical model of Ozeke *et al.* [2014] as our prototype model describes ground-based  
 545 power instead of total power in the equatorial azimuthal field. Instead we can briefly ex-  
 546 amine the properties of a  $Kp$ -based model of ground PSD, constructed similarly to the  
 547 solar wind model already presented. Ground-based PSD at 3.33 mHz, GILL is binned by  
 548 the corresponding  $Kp$  value and the probability distribution function is calculated in each  
 549 bin. These distributions are shown in Figure 9(a). By merging overlapping high  $Kp$  bins,  
 550 a parameterisation could be constructed where the distributions are distinct with relatively

551 small variance. Hence a  $Kp$ -based model based on sampling empirical probability distri-  
 552 bution functions could be constructed that satisfies point 2 of the necessary conditions for  
 553 a "good" parameterization in Section 4.2. However, it would not fully satisfy the require-  
 554 ment for forecasting or nowcasting capability (due to the 3-hr averaged nature of  $Kp$ ) or  
 555 the requirement for physically motivated parameters (it is difficult to ascribe a direct phys-  
 556 ical property to  $Kp$  due to the processing involved in constructing it, as discussed below).  
 557 The variance of the  $Kp$  bins are similar to those in our solar wind-parameterized model  
 558 (Figure 5); there may be a lower limit to the variance, either dependent on our hourly  
 559 timescale or due to underlying physical processes that require better characterization.

560 Interestingly, the variance of each  $Kp$  bin in this model (explicitly shown in Fig-  
 561 ure 9(b)) is clearly smaller than those from the storm-time data set used by *Murphy et al.*  
 562 [2016], even while the mean values are similar. The storm list used by *Murphy et al.* [2016]  
 563 is based on times where the magnetosphere is driven by corotating interaction regions and  
 564 coronal mass ejections, although part of the list was also constructed with a  $Dst$  thresh-  
 565 old. The greater uncertainty in the storm-time values (i.e. the larger variance) is there-  
 566 fore likely to be caused by more extreme solar wind conditions, while the similarity in  
 567 the mean values is most likely due to either a correlation between  $Dst$  and  $Kp$ , to the fact  
 568 that a portion of the storm list does not use a  $Dst$  threshold and so the internal conditions  
 569 of the magnetosphere may not be significantly different to the average, or most probably  
 570 a combination of the two. Regardless of the similar mean values, the increase in uncer-  
 571 tainty indicates that  $Kp$  does not capture ground ULF wave power behavior as well under  
 572 extreme solar wind conditions. It is likely that our model will perform better, being solar  
 573 wind based, but future work should quantify this.

574 To compare the  $Kp$ -based model directly to our solar wind based model, we have  
 575 used the  $Kp$  probability distribution functions to reproduce PSD values for the same time  
 576 series as Figure 3, shown in Figure 9(d). The time series is reasonably well followed by  
 577 both models, but forecasting skill scores indicate that the  $Kp$  model does not perform  
 578 quite as well as our solar wind based model. At GILL over the fifteen years, for 3.33 mHz  
 579 the solar wind based model has a positive skill value of 10.6 when compared to  $Kp$  as a  
 580 reference model. Nevertheless,  $Kp$  is a surprisingly good proxy for ground-based PSD.  
 581 Examining the relationship between  $Kp$  and the solar wind parameters suggests that  $Kp$   
 582 represents an independent contribution to power; the two-parameter plot in Figure 10  
 583 shows that median PSD increases with  $Kp$  independently of  $v_{sw}$ ,  $Bz$  or  $\log_{10}(\text{var}(Np))$ .

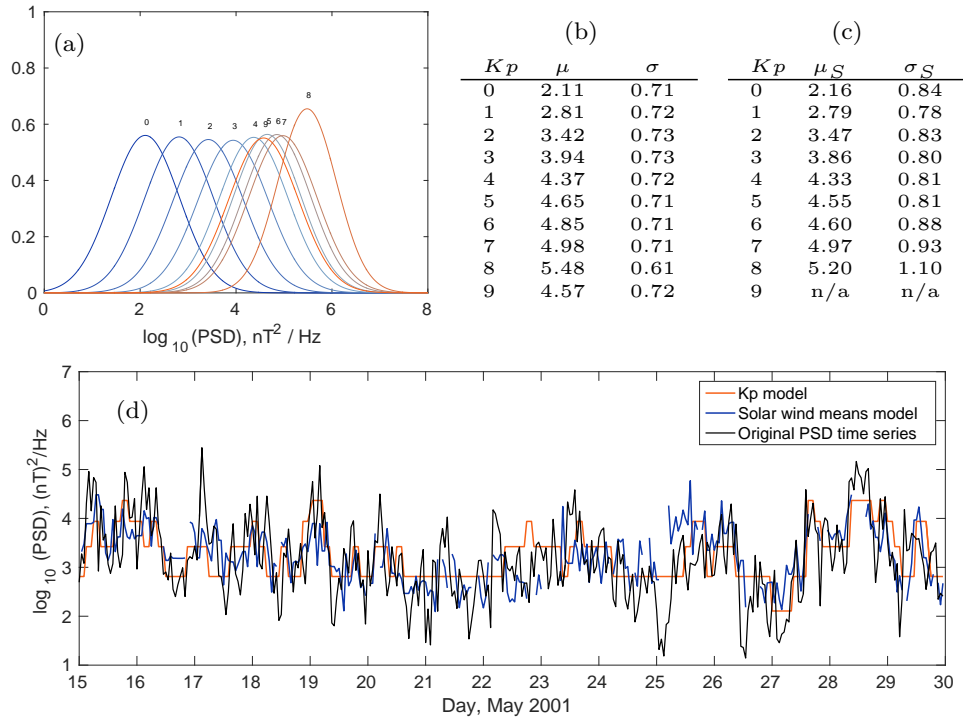
(This analysis is in line with that followed in Paper 1 to identify causally correlated parameters). As  $Kp$  is a mid-latitude index it is related to the magnetospheric convection electric field [Thomsen, 2004], while as a range index it is particularly related to explosive changes such as substorms. Since it is a three-hour index and substorm cycles generally last within three hours [Borovsky and Yakymenko, 2017],  $Kp$  is therefore related to substorm activity [Lockwood, 2013]. However, very large amplitude ULF waves may also contribute to  $Kp$ , as they may cause significant magnetic field deviations on the dayside stations used to construct  $Kp$ , particularly during times of low substorm activity. Hence the independent contribution indicated by  $Kp$  may represent substorm activity or ULF wave persistence. This suggests that ULF wave persistence should be studied, and that one of the first improvements to this prototype model should account for internal magnetospheric processes such as substorm activity. However, as  $Kp$  is highly averaged and processed, suitable options would be either a more physically based internal parameter, a solar wind time lag or the recent history of the magnetosphere. These different approaches will need to be considered for both their physical interpretability and their suitability for nowcasting and forecasting.

## 5 Other sources of uncertainty in radial diffusion coefficients

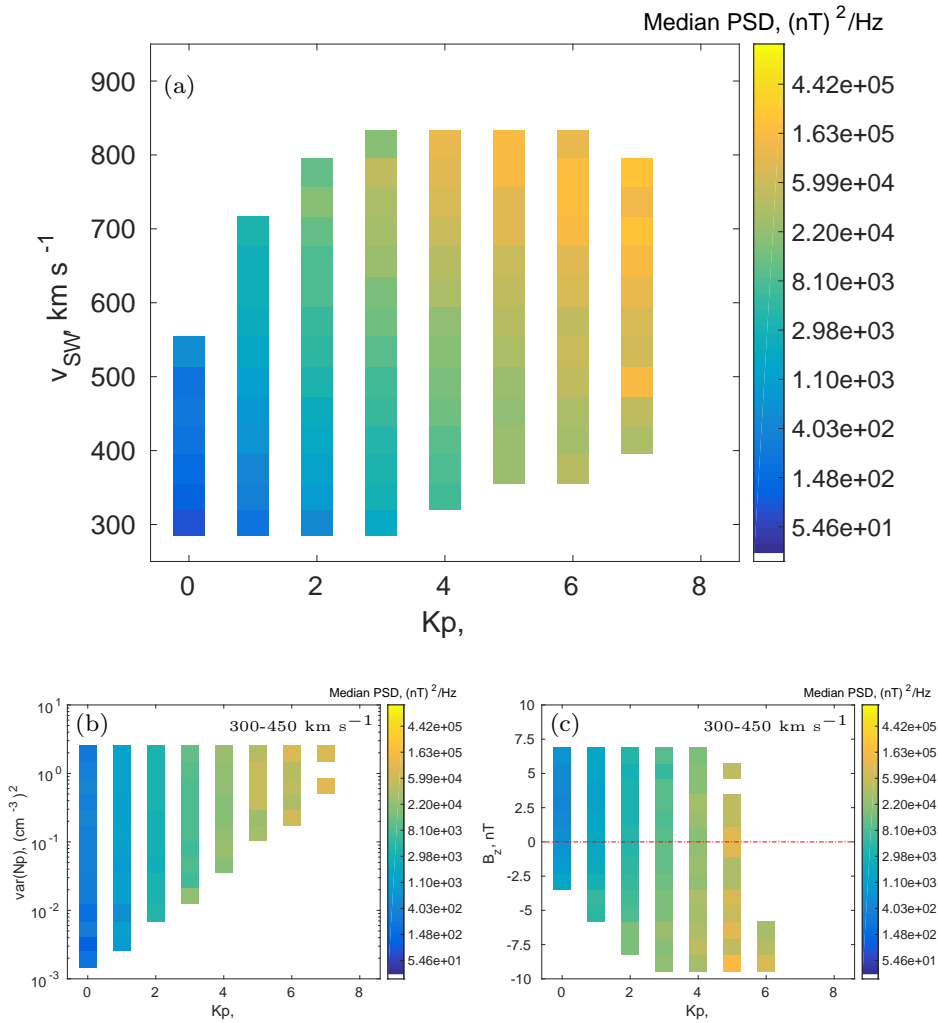
In this paper we have focused on a model of ULF wave PSD that will allow us to quantify the uncertainty introduced to calculation of radial diffusion coefficients. However, to construct a probabilistic description of diffusion coefficients we will need to include all sources of uncertainty; in this section additional sources of uncertainty are reviewed. Physical assumptions used in our theoretical formalism, constraints due to observational capabilities and different statistical methods all contribute to this uncertainty. Indeed, some sources of uncertainty have multiple knock-on effects such as the underlying magnetic field model, which can give rise to uncertainty in the formalism and again when calculating  $L^*$ , i.e. in processing observational data and when constructing averages for statistical wave maps.

The following review is ordered from purely physical assumptions, through approximations of theory that make up our formalism, to observational restrictions and finally uncertainty from our statistical model construction.

### 1. Background magnetic field model



600 **Figure 9.** A  $Kp$ -based model using probability distributions to predict ULF wave power at GILL,  $L \sim 6.6$ ,  
 601 3.33 mHz. (a) the fitted normal distributions of power for each  $Kp$  values, (b) the mean and standard deviation  
 602 of both these fits and (c) similar storm-time only fits. In (d) we use both the  $Kp$  and solar wind parameter  
 603 models to reproduce power over a short period of time (two weeks in May 2001, the same as Figure 3).



604 **Figure 10.** A series of "two-parameter" plots, where observations are binned by a solar wind parameter  
 605 and  $Kp$ , and the median power in each bin at GILL, 3.33 mHz is shown. (a) Power is binned by both speed  
 606 and  $Kp$ . Median ULF wave power is shown, which increases with both parameters. (b) Power is binned by  
 607 variance in proton number density  $Np$  and  $Kp$  for a single speed bin. Median ULF wave power increases with  
 608  $Kp$  but not with variance in number density. (c) Power is binned by  $B_z$  and  $Kp$  for a single solar wind speed.  
 609 Median ULF wave power increases with both  $B_z < 0$  and  $Kp$ . Hence  $Kp$  represents a contribution to median  
 610 ULF wave power independent of any correlations with solar wind speed,  $B_z$  or variance in proton number  
 611 density.

- 627 2. Other physics underlying the formalism  
 628 3. Summation over resonant frequencies  
 629 4. Accounting for azimuthal wave structure  
 630 5. Double-counting symmetric perturbations  
 631 6. Double-counting electric field perturbations  
 632 7. Methods of calculating power spectral density  
 633 8. Uncertainty from ground and space based observations  
 634 9. Statistical method construction

635 This list of known sources of uncertainty are all briefly reviewed below.

### 636 **5.1 Background magnetic field**

637 As discussed in Section 2, the diffusion coefficient  $D_{LL}$  can be derived from per-  
 638 turbations of electromagnetic fields. *Fälthammar* [1965] considered the radial diffusion  
 639 of equatorially mirroring particles due to small symmetric and asymmetric perturbations  
 640 of the dipole field, while others have extended this to other magnetic field models [*Schulz*  
 641 *and Eviatar*, 1969; *Elkington et al.*, 2003]. Clearly, the choice of magnetic field model will  
 642 contribute some uncertainty to the resulting diffusion coefficients, particularly at higher  
 643 radial distances and during geomagnetically extreme periods when magnetic field models  
 644 are often less accurate. This choice also gives rise to uncertainty in using observations, as  
 645 we map in situ observations from real space to  $L^*$ , or ground-based observations up to the  
 646 equatorial plane.

### 647 **5.2 Other physics underlying the formalism**

648 Diffusion coefficients are bounce-averaged and hence calculated in the equatorial  
 649 plane, using equatorially mirroring particles. This assumes that there is no latitude de-  
 650 pendent field variation such as the South Atlantic Anomaly. Additionally, the radial dif-  
 651 fusion coefficient used in radiation belt modelling is generally drift-averaged. However,  
 652 there is no conventional method of constructing a drift-averaged diffusion coefficient as it  
 653 is unclear whether it is more physically representative to calculate  $D_{LL}$  in each azimuthal  
 654 sector and average, or to calculate  $(\Delta L^*)^2$  in each sector, average these and then calculate  
 655  $D_{LL}$ . Instead, the lack of simultaneous measurements across a wide range of MLT sectors  
 656 often dictates our choice. Finally, we also note for completeness that an underlying phys-

ical assumption used in these derivations is that the frozen-in theorem is valid, i.e. that there is no parallel electric field [Falthammar, 1968].

### 5.3 Summation over resonant frequencies

Radial diffusion coefficients for a particle of a given energy are found in many existing formulations by evaluating the power at frequencies corresponding to the resonant and harmonic drift frequencies of a particle [Brautigam *et al.*, 2005; Fei *et al.*, 2006; Ozeke *et al.*, 2014; Ali *et al.*, 2016]. An example of this mechanism can be found by Elkington *et al.* [1999]. They showed that global toroidal mode ULF oscillations can accelerate electrons, particularly with the addition of a dawn-dusk electric field. However, integrating over a broader frequency range than just resonant frequencies results in larger final diffusion coefficients via a sum of smaller scatterings, where this frequency range is determined by the drift frequency and the sampling frequency (up to the bounce frequency limit) [Lejosne *et al.*, 2013]. Hence clarifying the role of resonant and non-resonant diffusion will be necessary to understand the energy dependence of diffusion coefficients.

When using the resonant frequency method, a common assumption used is that radial diffusion is caused by a magnetic impulse similar to a step function, so that power decays very slowly and is proportional to inverse square frequency,  $P \propto f^{-2}$ , [Schulz and Lanzerotti, 1974; Ozeke *et al.*, 2014]. This assumption is particularly useful as it causes the energy dependence of  $D_{LL}$  to cancel out and hence makes the diffusion coefficient easier to calculate. This approximation appears to be valid for average power spectra, but may not hold for the spectrum in an individual hour.

### 5.4 Accounting for azimuthal wave structure

Using observations to calculate  $D_{LL}$  via a sum over drift resonances involves yet more uncertainty in using and determining wave structures from in situ observations. Where our formalism sums only over resonant frequency contributions we must estimate the power at harmonics of that frequency. In their radial diffusion coefficient derivation, Fei *et al.* [2006] use a sum over azimuthal mode numbers  $m$  to describe this effect. However, in practice this is often simplified by assuming  $m = 1$ . Sarris and Li [2017] found that the amplitude of power is indeed concentrated in low  $m$ -numbers for the dayside and for less geomagnetically active time periods, but less so for the nightside and geomagnet-

687 ically active periods. *Murphy et al.* [2018] found that the  $m$ -number during a moderate  
688 storm is typically low but the distribution of positive or negative values depends on radial  
689 location; this initial study gives some idea how the direction of propagation (i.e.  $m < vs$   
690  $> 0$ ) is distributed among ULF waves but due to challenges in measuring  $m$  much more  
691 work is required. It is also unclear how direction of propagation should be included in ex-  
692 isting radial diffusion coefficient calculations, yet the orientation of these oscillations will  
693 clearly affect the resultant diffusion.

### 694 **5.5 Double-counting symmetric perturbations**

695 Another source of uncertainty that comes into both the theoretical framework and  
696 when using observations is double-counting from background magnetic field perturbations.  
697 This arises from the inclusion of both symmetric and asymmetric magnetic field pertur-  
698 bations, when only asymmetric (i.e. azimuthally dependent, or varying in magnetic local  
699 time) variations contribute to radial diffusion [*Fälthammar*, 1965; *Lejosne et al.*, 2012,  
700 2013]. While axisymmetric variations in the magnetic field may distort the entire drift  
701 contour (hence moving particles in real space) particles will not be moved to a new drift  
702 contour (i.e. changing the value of enclosed flux, or  $L^*$ ) without asymmetric perturba-  
703 tions. Observationally, it is difficult to identify asymmetric components from in situ data  
704 as it is generally a set of sparsely located point measurements, yet the asymmetric compo-  
705 nent is of smaller amplitude at the ground where there is better coverage of observations.  
706 This difficulty was resolved by *Lejosne et al.* [2012, 2013], who avoid the issue of confus-  
707 ing symmetric with asymmetric perturbations by using an analytical model of disturbances  
708 added to a dipole field. By sampling multiple in situ locations, the value of these addi-  
709 tional terms can be determined. *Lejosne et al.* [2013] also describes a method to approxi-  
710 mate this type of analysis using only single point measurements, which reduces the num-  
711 ber of spacecraft coverage necessary to cover the  $L^*$ -shells and sectors of interest. While  
712 this approach removes symmetric double-counting, uncertainty remains from the use of a  
713 dipole field model. This emphasises the necessity of calculating uncertainty to allow us to  
714 choose between physical assumptions in diffusion coefficient estimation methods.

### 715 **5.6 Double-counting electric field perturbations**

716 The second type of double counting arises from our treatment of electric fields.  
717 Theoretically, if the inductive electric field term is neglected from the magnetic com-



718 ponent of diffusion  $D_{LL}^B$ , adiabatic changes in the magnetic field may appear to result  
 719 in spurious changes in  $L^*$  and hence in our radial diffusion coefficients [Fälthammar,  
 720 1965]. However, it is difficult to quantify this term as in situ observations simply pro-  
 721 vide the localised value of the electric field, and it is difficult to distinguish how much of  
 722 that is due to induction (i.e.  $\frac{dB}{dt}$ ). Hence any diffusion coefficient calculation is at risk of  
 723 double-counting electromagnetic field contributions. Using the method briefly mentioned  
 724 in the previous section, Lejosne *et al.* [2012, 2013] also address this inductive electric field  
 725 double-counting. More commonly, simplifying assumptions are made to make this prob-  
 726 lem more tractable. Fei *et al.* [2006] simply sum the electric and magnetic components  
 727  $D_{LL} = D_{LL}^E + D_{LL}^B$ . This approach is approximately valid where either the two electric  
 728 components can be distinguished, (for example by making assumptions on the background  
 729 magnetic field model and the types of wave present, which determines the relationship be-  
 730 tween the electric and magnetic field perturbations, [Ozeke *et al.*, 2012]) or when either  
 731  $D_{LL}^E \ll D_{LL}^B$  or  $D_{LL}^B \ll D_{LL}^E$ . However, these coefficients may be of comparable magni-  
 732 tude [Pokhotelov *et al.*, 2016] so it is unclear how often this approximation can be used.

### 733 **5.7 Methods of calculating power spectral density**

734 While power spectral density is vital to our diffusion coefficient derivations, there  
 735 are multiple valid transforms between the time and frequency domain. Different transform  
 736 methods are better suited for either broadband or narrowband signals and so may over or  
 737 underestimate the power at a single frequency, hence the choice of transform should reflect  
 738 either the drift-resonant sum or frequency-range integral method of coefficient derivation.  
 739 For example, if  $D_{LL}$  is calculated at specific resonant frequencies, then different methods  
 740 of calculating power spectral density could result in different amounts of diffusion. Addi-  
 741 tionally, the underlying assumptions of a transformation to the frequency domain via the  
 742 Wiener-Khinchin theorem have not been fully explored, such as stationarity on a range of  
 743 timescales. It is not clear whether this would contribute uncertainty to the final diffusion  
 744 coefficients but is included here for completeness.

### 745 **5.8 Uncertainty from ground and space based observations**

746 Some types of uncertainty are unique to the observation method. While the real-  
 747 space location of in situ data may be known, it is difficult to be certain of the  $L^*$ -value.  
 748 Spacecraft are often located at the equator and therefore may be at the node of any res-

749 onant field line oscillations, which they will therefore underestimate. As point measure-  
750 ments, it is difficult to make assumptions about the spatial and temporal scale of oscilla-  
751 tions from single spacecraft measurements. However, ground-based data has its own set of  
752 uncertainties; each ground station corresponds to some field-line centred volume of vari-  
753 able width, and the mapping of ground power to the equatorial plane relies on assump-  
754 tions of ionospheric conductivity and number density variations along the field, in addition  
755 to the magnetic field model and  $E_{\parallel} = 0$  approximations discussed previously [Ozeke *et al.*,  
756 2009].

## 757 **5.9 Statistical model construction**

758 When constructing statistical models of diffusion coefficients, additional uncertainty  
759 enters due to our methods of averaging and parameterization. For example, while az-  
760 imuthal resolution is important for statistical wave maps as it is the asymmetric (azimuthally  
761 dependent) contributions that account for radial diffusion, it is unclear what size azimuthal  
762 sector to average over as the spatial coherence of ULF waves has not been studied for this  
763 purpose. Similarly, the plasma density distribution affects the occurrence and penetration  
764 of ULF waves and hence radial diffusion. Averaging over periods with both high and low  
765 density will introduce more variability in statistical models.

766 Finally, the method of constructing a statistical model can also introduce uncertainty  
767 by our choice of parameters. Several recent studies calculating diffusion coefficients across  
768 the magnetosphere parameterize by  $Kp$  and  $L$  [Ozeke *et al.*, 2014; Lejosne *et al.*, 2013;  
769 Brautigam and Albert, 2000; Brautigam *et al.*, 2005; Ali *et al.*, 2016; Liu *et al.*, 2016]. Us-  
770 ing  $L$  as a parameter is fraught with difficulty due to the difficulty mapping  $L$  to  $L^*$ . The  
771 quality of such a parameterization can be quantified by examining the fits and the choice  
772 of parameters, as discussed in Section 4.1.

## 773 **5.10 Summary**

774 There are many sources of uncertainty in our existing methods of calculating dif-  
775 fusion coefficients. Quantifying the uncertainty introduced by different theoretical for-  
776 malisms and by different physical assumptions will aid in selecting the most appropriate  
777 model approach with minimal uncertainty. Uncertainty due to observational restrictions,  
778 underlying natural variation and due to statistical methods may not be as easily avoided

779 but still needs to be quantified in order to accurately describe the ability of radial diffusion  
780 coefficients to reproduce radiation belt phenomena in modeling. In this paper we have fo-  
781 cused on producing a statistical model of ULF power spectral density that is suitable for  
782 nowcasting and forecasting yet can capture the uncertainty due to underlying natural vari-  
783 ation. This is only one component of a final, fully probabilistic radial diffusion coefficient  
784 model. Until then it can be used to improve existing models and to better understand the  
785 physics underlying the generation and propagation of ULF waves.

## 786 **6 Conclusion**

787 A description of ULF wave power is an important component of any radial diffu-  
788 sion coefficient calculation. We have outlined a method to construct a model of ground-  
789 based ULF wave power that is dependent on solar wind parameters, azimuthal angle (i.e.  
790 magnetic local time), station latitude and frequency. This model outputs probability dis-  
791 tributions, which will allow us to produce probabilistic forecasts and to identify areas of  
792 uncertainty in future statistical models of radial diffusion coefficients.

793 The probability distribution in each bin is approximated by a normal distribution of  
794 log-power, which allows us to use two methods of predicting ULF wave power. By look-  
795 ing up the appropriate normal distribution corresponding to solar wind observations in a  
796 given hour, that distribution can either be sampled or the mean can be taken. Sampling  
797 each distribution is suitable for reproducing the total distribution of power over an ex-  
798 tended event while using the mean value is the best method of reproducing a time series.  
799 Comparing this to a similarly constructed model based on  $Kp$ , we find that our prototype  
800 model based only on three solar wind parameters slightly outperforms the  $Kp$  model and  
801 that  $Kp$  represents an independent contribution to power that should later be included in  
802 our model. We also find that the uncertainty in a  $Kp$  parameterization increases during  
803 storm times. Hence future improvements could include a dependence on internal magne-  
804 topheric properties that satisfy the characteristics of a "good" parameterization, which we  
805 have defined in Section 4.1.

806 To apply this prototype model to the production of radial diffusion coefficients in-  
807 volves extending to more stations and mapping ground based power to the equatorial elec-  
808 tric field [Ozeke *et al.*, 2009, 2012], then examining whether this is an effective model and  
809 where the largest uncertainty stems from. Identifying the source of this uncertainty will

810 allow for targeted improvement of a statistical radial diffusion coefficient model. In Sec-  
811 tion 5 we reviewed other ways that uncertainty can enter the radial diffusion coefficient  
812 calculation in addition to the underlying wave model. We anticipate that the methods and  
813 tests outlined throughout this paper can be used to inform construction of other compo-  
814 nents of a fully probabilistic radial diffusion coefficient model.

815 Future improvements to reduce any uncertainty from the solar wind based model  
816 outlined here could be made by including time-lagged solar wind contributions, substorms,  
817 magnetospheric plasma density, magnetospheric conditions and also the time history of  
818 the magnetosphere. Additionally, the underlying normal distribution approximation could  
819 be further examined to identify where this approximation holds; as well as quantifying the  
820 resulting uncertainty this will indicate magnetospheric regions or solar wind conditions of  
821 physical interest for the generation and propagation of ULF waves.

822 To summarize, our simple parameterization based on magnetospheric regions and  
823 just three solar wind properties predicts ULF wave power time series better than assuming  
824 that power carries on from the previous hour. We submit that this is a surprisingly effec-  
825 tive result for such a simple model and therefore constitutes a step towards a probabilistic  
826 model of radial diffusion coefficients. This prototype model can also be used to investigate  
827 questions about the occurrence of ULF waves; immediate future work includes examining  
828 the parameterization results across a variety of stations and MLT sectors.

## 829 **Acknowledgments**

830 The authors gratefully acknowledge use of NASA/GSFC's Space Physics Data Facility  
831 OMNIWeb service and OMNI data, and the use of data from the CANOPUS/CARISMA  
832 magnetometer array ([www.carisma.ca](http://www.carisma.ca)) which is operated by the University of Alberta  
833 and funded by the Canadian Space Agency. SNB receives funding from the Natural En-  
834 vironment Research Council as part of the SCENARIO Doctoral Training Partnership  
835 NE/L002566/1. CEJW is supported by STFC grant ST/R000921/1 and NERC grant NE/P017274/1.  
836 IJR is supported by NERC grant NE/P017185/1 and STFC grant ST/N000722/1. MJO and  
837 ML are supported by STFC consolidated grant number ST/M000885/1 and the SWIGS  
838 NERC Directed Highlight Topic Grant number NE/P016928/1/. KRM is partial-funded by  
839 NSF grant 1602403 and JKS is supported by STFC consolidated grant ST/N0007722/1  
840 and NERC grant NE/L007495/1. The authors would like to thank additional members  
841 of the NERC Rad-Sat consortium for useful discussions, and SNB would like to thank

842 Solène Lejosne for discussions that refined this work. The statistical model constructed  
843 using the methods outlined in this article is available from the University of Reading Re-  
844 search Data Archive, <http://dx.doi.org/10.17864/1947.190>.

## 845 References

846 Ali, A. F., D. M. Malaspina, S. R. Elkington, A. N. Jaynes, A. A. Chan, J. Wygant, and  
847 C. A. Kletzing (2016), Electric and magnetic radial diffusion coefficients using the Van  
848 Allen probes data, *Journal of Geophysical Research: Space Physics*, *121*(10), 9586–  
849 9607, doi:10.1002/2016JA023002.

850 Baker, D. N., R. D. Belian, P. R. Higbie, R. W. Klebesadel, and J. B. Blake (1987), Deep  
851 dielectric charging effects due to high-energy electrons in earth's outer magnetosphere,  
852 *Journal of Electrostatics*, *20*(1), 3–19, doi:10.1016/0304-3886(87)90082-9.

853 Bentley, S. N. (2019), A probabilistic, empirical model of magnetospheric ultra-low fre-  
854 quency wave power., doi:10.17864/1947.190, University of Reading Research Data  
855 Archive. (dataset).

856 Bentley, S. N., C. E. J. Watt, M. J. Owens, and I. J. Rae (2018), ULF Wave Activity  
857 in the Magnetosphere: Resolving Solar Wind Interdependencies to Identify Driving  
858 Mechanisms, *Journal of Geophysical Research: Space Physics*, *123*(4), 2745–2771, doi:  
859 10.1002/2017JA024740.

860 Berner, J., U. Achatz, L. Batté, L. Bengtsson, A. De La Cámara, H. M. Christensen,  
861 M. Colangeli, D. R. Coleman, D. Crommelin, S. I. Dolaptchiev, C. L. Franzke,  
862 P. Friederichs, P. Imkeller, H. Järvinen, S. Juricke, V. Kitsios, F. Lott, V. Lucarini,  
863 S. Mahajaajaajan, T. N. Palmer, C. Penland, M. Sakradzijaja, J. S. Von Storch,  
864 A. Weisheimer, M. Weniger, P. D. Williams, and J. I. Yano (2017), Stochastic param-  
865 eterization toward a new view of weather and climate models, *Bulletin of the American*  
866 *Meteorological Society*, *98*(3), 565–587, doi:10.1175/BAMS-D-15-00268.1.

867 Borovsky, J. E., and K. Yakymenko (2017), Substorm occurrence rates, substorm recur-  
868 rence times, and solar wind structure, *Journal of Geophysical Research: Space Physics*,  
869 *122*(3), 2973–2998, doi:10.1002/2016JA023625.

870 Brautigam, D. H., and J. M. Albert (2000), Radial diffusion analysis of outer radiation belt  
871 electrons during the October 9, 1990, magnetic storm, *Journal of Geophysical Research:*  
872 *Space Physics*, *105*(A1), 291–309, doi:10.1029/1999JA900344.

- 873 Brautigam, D. H., G. P. Ginet, J. M. Albert, J. R. Wygant, D. E. Rowland, A. Ling,  
874 and J. Bass (2005), CRRES electric field power spectra and radial diffusion co-  
875 efficients, *Journal of Geophysical Research: Space Physics*, 110(A2), 1–15, doi:  
876 10.1029/2004JA010612.
- 877 Cohen, J. (1988), *Statistical Power Analysis for the Behavioral Sciences*, 2nd ed ed., 567  
878 pp., Erlbaum, Hillsdale, N.J.
- 879 Elkington, S. R. (2013), *A Review of ULF Interactions with Radiation Belt Electrons*, pp.  
880 177–193, American Geophysical Union (AGU), doi:10.1029/169GM12.
- 881 Elkington, S. R., M. K. Hudson, and A. A. Chan (1999), Acceleration of relativistic elec-  
882 trons via drift-resonant interaction with toroidal-mode Pc-5 ULF oscillations, *Geophysi-  
883 cal Research Letters*, 26(21), 3273–3276, doi:10.1029/1999GL003659.
- 884 Elkington, S. R., M. K. Hudson, and A. A. Chan (2003), Resonant acceleration and diffu-  
885 sion of outer zone electrons in an asymmetric geomagnetic field, *Journal of Geophysical  
886 Research: Space Physics*, 108(A3), 1–15, doi:10.1029/2001JA009202.
- 887 Fälthammar, C.-G. (1965), Effects of Time-Dependent Electric Fields on Geomagnetically  
888 Trapped Radiation, *J. Geophys. Res.*, 70(11), 2503–2516, doi:10.1029/JZ070i011p02503.
- 889 Fälthammar, C.-G. (1968), Radial Diffusion by Violation of the Third Adiabatic Invariant,  
890 in *Earth's Particles and Fields, Proceedings of the NATO Advanced Study Institute, July  
891 31-August 11, 1967*, edited by B. McCormac, pp. 157–169, Reinhold Book Corporation,  
892 Chicago, Illinois.
- 893 Fei, Y., A. A. Chan, S. R. Elkington, and M. J. Wiltberger (2006), Radial diffusion  
894 and MHD particle simulations of relativistic electron transport by ULF waves in the  
895 September 1998 storm, *Journal of Geophysical Research*, 111(A12), A12,209, doi:  
896 10.1029/2005JA011211.
- 897 Frederickson, A. R. (1996), Correction to ???Upsets Related to Spacecraft Charging???,  
898 *IEEE Transactions on Nuclear Science*, 43(4), 2454, doi:10.1109/TNS.1996.531795.
- 899 Gjerloev, J. W. (2012), The SuperMAG data processing technique, *Journal of Geophysical  
900 Research: Space Physics*, 117(9), 1–19, doi:10.1029/2012JA017683.
- 901 Horne, R. B., S. A. Glauert, N. P. Meredith, D. Boscher, V. Maget, D. Heynderickx,  
902 and D. Pitchford (2013), Space weather impacts on satellites and forecasting the  
903 Earth's electron radiation belts with SPACECAST, *Space Weather*, 11(4), 169–186, doi:  
904 10.1002/swe.20023.

- 905 Jacobs, J. A., Y. Kato, S. Matsushita, and V. A. Troitskaya (1964), Classification of Geo-  
906 magnetic Micropulsations, *Geophysical Journal of the Royal Astronomical Society*, 8(3),  
907 341–342, doi:10.1029/JZ069i001p00180.
- 908 Kepko, L., H. E. Spence, and H. J. Singer (2002), ULF waves in the solar wind as direct  
909 drivers of magnetospheric pulsations, *Geophysical Research Letters*, 29(8), 39–1–39–4,  
910 doi:10.1029/2001GL014405.
- 911 King, J. H., and N. E. Papitashvili (2005), Solar wind spatial scales in and comparisons  
912 of hourly Wind and ACE plasma and magnetic field data, *Journal of Geophysical Re-*  
913 *search: Space Physics*, 110(A2), 1–9, doi:10.1029/2004JA010649.
- 914 Lejosne, S., D. Boscher, V. Maget, and G. Rolland (2012), Bounce-averaged approach to  
915 radial diffusion modeling: From a new derivation of the instantaneous rate of change of  
916 the third adiabatic invariant to the characterization of the radial diffusion process, *Jour-*  
917 *nal of Geophysical Research: Space Physics*, 117(8), 1–10, doi:10.1029/2012JA018011.
- 918 Lejosne, S., D. Boscher, V. Maget, and G. Rolland (2013), Deriving electromagnetic radial  
919 diffusion coefficients of radiation belt equatorial particles for different levels of mag-  
920 netic activity based on magnetic field measurements at geostationary orbit, *Journal of*  
921 *Geophysical Research: Space Physics*, 118(6), 3147–3156, doi:10.1002/jgra.50361.
- 922 Liu, W., W. Tu, X. Li, T. Sarris, Y. Khotyaintsev, H. Fu, H. Zhang, and Q. Shi (2016), On  
923 the calculation of electric diffusion coefficient of radiation belt electrons with in situ  
924 electric field measurements by THEMIS, *Geophysical Research Letters*, 43(3), 1023–  
925 1030, doi:10.1002/2015GL067398.
- 926 Lockwood, M. (2013), Reconstruction and Prediction of Variations in the Open Solar  
927 Magnetic Flux and Interplanetary Conditions, *Living Reviews in Solar Physics*, 10, doi:  
928 10.12942/lrsp-2013-4.
- 929 Loto'aniu, T. M., H. J. Singer, C. L. Waters, V. Angelopoulos, I. R. Mann, S. R. Elking-  
930 ton, and J. W. Bonnell (2010), Relativistic electron loss due to ultralow frequency waves  
931 and enhanced outward radial diffusion, *Journal of Geophysical Research: Space Physics*,  
932 115(12), 1–13, doi:10.1029/2010JA015755.
- 933 Mann, I. R., D. K. Milling, I. J. Rae, L. G. Ozeke, A. Kale, Z. C. Kale, K. R. Murphy,  
934 A. Parent, M. Usanova, D. M. Pahud, E. A. Lee, V. Amalraj, D. D. Wallis, V. An-  
935 gelopoulos, K. H. Glassmeier, C. T. Russell, H. U. Auster, and H. J. Singer (2008), *The*  
936 *upgraded CARISMA magnetometer array in the THEMIS era*, vol. 141, 413–451 pp., doi:  
937 10.1007/s11214-008-9457-6.

- 938 McPherron, R. L. (2005), Magnetic pulsations: Their sources and relation to solar wind  
939 and geomagnetic activity, *Surveys in Geophysics*, 26(5), 545–592, doi:10.1007/s10712-  
940 005-1758-7.
- 941 Murphy, K. R., I. R. Mann, I. J. Rae, and D. K. Milling (2011), Dependence of  
942 ground-based Pc5 ULF wave power on F10.7 solar radio flux and solar cycle phase,  
943 *Journal of Atmospheric and Solar-Terrestrial Physics*, 73(11-12), 1500–1510, doi:  
944 10.1016/j.jastp.2011.02.018.
- 945 Murphy, K. R., I. R. Mann, I. J. Rae, D. G. Sibeck, and C. E. J. Watt (2016), Accurately  
946 characterizing the importance of wave-particle interactions in radiation belt dynamics:  
947 The pitfalls of statistical wave representations, *Journal of Geophysical Research: Space*  
948 *Physics*, 121(8), 7895–7899, doi:10.1002/2016JA022618.
- 949 Murphy, K. R., A. R. Inglis, D. G. Sibeck, I. J. Rae, C. E. J. Watt, M. Silveira,  
950 F. Plaschke, S. G. Claudepierre, and R. Nakamura (2018), Determining the mode,  
951 frequency, and azimuthal wave number of ULF waves during a HSS and mod-  
952 erate geomagnetic storm, *Journal of Geophysical Research: Space Physics*, doi:  
953 10.1029/2017JA024877.
- 954 Owens, M. J., R. Challen, J. Methven, E. Henley, and D. R. Jackson (2013), A 27  
955 day persistence model of near-Earth solar wind conditions: A long lead-time fore-  
956 cast and a benchmark for dynamical models, *Space Weather*, 11(5), 225–236, doi:  
957 10.1002/swe.20040.
- 958 Ozeke, L. G., I. R. Mann, and I. J. Rae (2009), Mapping guided Alfvén wave mag-  
959 netic field amplitudes observed on the ground to equatorial electric field amplitudes  
960 in space, *Journal of Geophysical Research: Space Physics*, 114(A1), n/a–n/a, doi:  
961 10.1029/2008JA013041.
- 962 Ozeke, L. G., I. R. Mann, K. R. Murphy, I. J. Rae, D. K. Milling, S. R. Elkington,  
963 A. A. Chan, and H. J. Singer (2012), ULF wave derived radiation belt radial diffu-  
964 sion coefficients, *Journal of Geophysical Research: Space Physics*, 117(4), 1–16, doi:  
965 10.1029/2011JA017463.
- 966 Ozeke, L. G., I. R. Mann, K. R. Murphy, I. Jonathan Rae, and D. K. Milling (2014), An-  
967 alytic expressions for ULF wave radiation belt radial diffusion coefficients, *Journal of*  
968 *Geophysical Research: Space Physics*, 119(3), 1587–1605, doi:10.1002/2013JA019204.
- 969 Pokhotelov, D., I. J. Rae, K. R. Murphy, and I. R. Mann (2016), Effects of ULF wave  
970 power on relativistic radiation belt electrons: 8–9 October 2012 geomagnetic storm,



- 971 *Journal of Geophysical Research: Space Physics*, 121(12), 11,766–11,779, doi:  
972 10.1002/2016JA023130.
- 973 Rae, I. J., I. R. Mann, K. R. Murphy, L. G. Ozeke, D. K. Milling, A. A. Chan, S. R. Elk-  
974 ington, and F. Honary (2012), Ground-based magnetometer determination of in situ  
975 Pc4-5 ULF electric field wave spectra as a function of solar wind speed, *Journal of*  
976 *Geophysical Research: Space Physics*, 117(A4), n/a–n/a, doi:10.1029/2011JA017335.
- 977 Richardson, J. D., and K. I. Paularena (1998), The orientation of plasma structure in the  
978 solar wind, *Geophysical Research Letters*, 25(12), 2097–2100, doi:10.1029/98GL01520.
- 979 Roederer, J. G., and H. Zhang (2014), *Dynamics of Magnetically Trapped Particles*, vol.  
980 403, doi:10.1007/978-3-642-41530-2.
- 981 Rostoker, G., J. C. Samson, F. Creutzberg, T. J. Hughes, D. R. McDiarmid, A. G. McNa-  
982 mara, A. V. Jones, D. D. Wallis, and L. L. Cogger (1995), Canopus - A ground-based  
983 instrument array for remote sensing the high latitude ionosphere during the ISTP/GGS  
984 program, *Space Science Reviews*, 71(1-4), 743–760, doi:10.1007/BF00751349.
- 985 Rostoker, G., S. Skone, and D. N. Baker (1998), On the origin of relativistic electrons in  
986 the magnetosphere associated with some geomagnetic storms, *Geophysical Research*  
987 *Letters*, 25(19), 3701, doi:10.1029/98GL02801.
- 988 Saito, T. (1969), Geomagnetic Pulsations, *Space Science Reviews*, 10(3), 319–412, doi:  
989 10.1007/bf00203620.
- 990 Sandhu, J. K., T. K. Yeoman, M. K. James, I. J. Rae, and R. C. Fear (2018), Variations  
991 of High-Latitude Geomagnetic Pulsation Frequencies: A Comparison of Time-of-Flight  
992 Estimates and IMAGE Magnetometer Observations, *Journal of Geophysical Research:*  
993 *Space Physics*, 123(1), 567–586, doi:10.1002/2017JA024434.
- 994 Sarris, T. E., and X. Li (2017), Geomagnetic activity and local time dependence of the  
995 distribution of ultra low-frequency wave power in azimuthal wavenumbers, *m, Annales*  
996 *Geophysicae*, 35(3), 629–638, doi:10.5194/angeo-35-629-2017.
- 997 Schulz, M., and A. Eviatar (1969), Diffusion of equatorial particles in the outer  
998 radiation zone, *Journal of Geophysical Research*, 74(9), 2182–2192, doi:  
999 10.1029/JA074i009p02182.
- 1000 Schulz, M., and L. J. Lanzerotti (1974), *Particle Diffusion in the Radiation Belts, Physics*  
1001 *and Chemistry in Space*, vol. 7, Springer Berlin Heidelberg, Berlin, Heidelberg, doi:  
1002 10.1007/978-3-642-65675-0.

- 1003 Southwood, D. J., and M. G. Kivelson (1990), The magnetohydrodynamic response of  
1004 the magnetospheric cavity to changes in solar wind pressure, *Journal of Geophysical*  
1005 *Research*, 95(A3), 2301, doi:10.1029/JA095iA03p02301.
- 1006 Tanskanen, E. I. (2009), A comprehensive high-throughput analysis of substorms observed  
1007 by IMAGE magnetometer network: Years 1993-2003 examined, *Journal of Geophysical*  
1008 *Research: Space Physics*, 114(5), 1–11, doi:10.1029/2008JA013682.
- 1009 Thomsen, M. F. (2004), Why Kp is such a good measure of magnetospheric convection,  
1010 *Space Weather*, 2(11), n/a–n/a, doi:10.1029/2004SW000089.
- 1011 Turner, D. L., Y. Shprits, M. Hartinger, and V. Angelopoulos (2012), Explaining sudden  
1012 losses of outer radiation belt electrons during geomagnetic storms, *Nature Physics*, 8(3),  
1013 208–212, doi:10.1038/nphys2185.
- 1014 Waters, C. L., F. W. Menk, and B. J. Fraser (1991), The resonance structure of low lat-  
1015 itude pc3 geomagnetic pulsations, *Geophysical Research Letters*, 18(12), 2293–2296,  
1016 doi:10.1029/91GL02550.
- 1017 Watt, C. E., I. J. Rae, K. R. Murphy, C. Anekallu, S. N. Bentley, and C. Forsyth  
1018 (2017), The parameterization of wave-particle interactions in the Outer Radiation  
1019 Belt, *Journal of Geophysical Research: Space Physics*, 122(9), 9545–9551, doi:  
1020 10.1002/2017JA024339.
- 1021 Weimer, D. R., D. M. Ober, N. C. Maynard, W. J. Burke, M. R. Collier, D. J. McComas,  
1022 N. F. Ness, and C. W. Smith (2002), Variable time delays in the propagation of the in-  
1023 terplanetary magnetic field, *J. Geophys. Res.*, 107(1), doi:10.1029/2001ja009102.
- 1024 West Jun, H. I., R. M. Buck, and J. R. Walton (1972), Shadowing of Electron Azimuthal-  
1025 Drift Motions near the Noon Magnetopause, doi:10.1038/physci240006a0.